UNIVERSITÀ DEGLI STUDI DI NAPOLI
FEDERICO II

FACOLTÀ DI INGEGNERIA
Dipartimento di Meccanica ed Energetica

DOTTORATO DI RICERCA
INGEGNERIA DEI SISTEMI MECCANICI
XXV CICLO

Aeroacoustic Methods for Low-Noise Technologies Design

COORDINATOR OF THE PHD SCHOOL:
Prof. Fabio Bozza

TUTORS:
Prof. Raffaele Tuccillo
Ing. Lorenzo Notarnicola

CANDIDATE:
Ing. Mattia Barbarino

Acknowledgments

I am particularly grateful to Dr. Damiano Casalino for the fruitful cooperation during his stay at CIRA and for his essential guidance on numerics and aeroacoustics.

I would like to thank Ing. Paolo Di Francescantonio for his many useful suggestions on the Boundary Element Method.

I would like also to thank Prof. Raffaele Tuccillo, Ing. Lorenzo Notarnicola, Dr. Piergiovanni Renzoni and my colleagues at CIRA for their review of the thesis and for their support and encouragement.

Abstract

As environmental concerns are gaining increased public attention and with the rapid growth of air traffic foreseen in the forthcoming years, the scientific community and aircraft manufacturers are devoting significant resources in developing fast and reliable methods to deliver low noise design solutions.

Since fully-resolved Navier–Stokes equations (DNS), and even filtered Navier-Stokes equations such as LES and DES methods, are still too computationally demanding for real applications, the present dissertation is focused on the theoretical and numerical formulation of different alternative computational aeroacoustic methods and their application to typical aeronautics low noise design problems.

Following an introduction about the theoretical formulation of the Acoustic Analogy approach based on the Lighthill's equation, the thesis is focused on the development of a Boundary Element Method (BEM) based on the convective wave equation for uniform mean flow.
The BEM code kernel, developed for managing hybrid unstructured grids, builds up the global system matrix by assembling different matrix blocks for the governing equations and the boundary conditions. This strategy allows a more general and efficient implementation of the boundary conditions.
The BEM code is also validated against classical analytical test cases for both internal and external problems.

Moreover, the broadband noise generated by aircraft surfaces (Airframe noise) is presented with particular attention devoted to the development of RANS-based models for source field characterization.

Finally the application of the developed methods to the analysis of the Landing Gear low-noise design problem is presented.

Contents

List of Figures

List of Tables

1. Context

Aviation is an essential element of today's global society. With 2.8 billion passengers yearly and $539 billion of world gross domestic product (GDP) generated per year, aviation brings people and cultures together and significantly contributes to the economic growth [1].

Due to the continuous and steady growth of air traffic, the aircraft manufacturers pose a growing interest to environmental issues like pollution, noise impact and climate change.

In particular, as airports are often close to urban areas, people are often exposed to significant noise levels, radiated from airplanes especially during approach and take-off. Due to the significant noise produced, aircraft operations are bound by strict regulations. Only aircrafts that comply with these regulations are allowed to takeoff or land.

In this context, manufacturers need to adhere to noise regulations and have thus a great interest in reducing the noise levels radiated by their aircrafts. For this reason, they have increasingly considered aeroacoustic phenomena and mechanisms of sound generation and propagation as a relevant design parameter.

Considering the growing social awareness of environmental issues the European Commission recently devoted significant funding to Research Programmes with the aim of developing new technologies able to reduce the environmental impact of the air transport system.
Most of the developments presented in this thesis have been set up in the framework of the European Commission funded Clean-Sky programme. The Clean-Sky Joint Technology Initiative is a Public Private Partnership between the European Commission and the Aeronautical Industry that was established with the aim of developing aviation technologies compliant with increasingly stringent pollutant emissions and noise reduction goals.

2. Introduction

2.1. Background and Motivation

In the context of Computational Fluid Dynamics (CFD), the application of Direct Numerical Simulation (DNS) to aeroacoustics is becoming more feasible with the growing advancement in computational resources.
However, due to the large disparities of length and energy scales between fluid and acoustic fields, the use of fully-solved Navier–Stokes equations without turbulence modeling (DNS) is still restricted to low Reynolds number flows.

The numerical simulation of aeroacoustics through the solution of filtered Navier Stokes equations, either using fully large-eddy simulation (LES) or hybrid RANS LES approaches such as the detached-eddy simulation (DES), is a major area of research. However, despite the increase in computational power, even these types of simulations are not yet feasible for industrial purposes.
Indeed, industry interest is mainly devoted to reliable numerical tools to be applied to realistic configurations for re-design of old configurations and for the development of new technologies. Furthermore the growing interest on multi-disciplinary and multi-objective optimization necessarily lead to approaches that require low computational time.
Therefore, Reynolds-Averaged Navier-Stokes (RANS) simulations still remain the more feasible approach for CFD applications of industrial interest. However, RANS computations alone are not able to model the aeroacoustic phenomena.

The Acoustic Analogy approach, introduced by James Lighthill in 1952 [2,3], along with the recent development and improvement of RANS-based methods for turbulent field synthesis, constitute a valid alternative to LES or DES for noise prediction.
The Acoustic Analogy approach allows to divide the computational domain into a non–linear source region and a wave propagation region.
The turbulent unsteady flow is considered confined in the source region and used as a forcing input of the acoustic propagation. It is straightforward to underline that the

direct counterpart of the main assumption of the Acoustic Analogy is that no physical feedback occurs from the acoustic propagation to the flow field.

Among the Acoustic Analogy methods, integral methods are widely used in CAA for solving open domains. (as Lighthill's acoustic equation [2,3] and Ffwocs Williams and Hawkings formulation [4]). Despite these methods don't require the volume discretization, they don't allow treating confined aeroacoustic problems, where solid boundaries are present.
Different techniques of volume discretization are available in the literature, as discontinuous Galerkin (DG), finite volume (FV) method and Finite Element (FE) method accounting for scattering in uniform and non-uniform mean flows.
At last, Boundary Element methods (BEM) deserves a particular classification since it accounts for the interactions with solid surfaces discretizing only the solid surfaces. The main advantage of the BEM approach is the reduced time required for the generation of the computational grid. On the other hand, it leads to a dense system matrix that would require special algorithms, as Fast Multipole Methods (FMM), to reduce memory and computational time.

Concerning the turbulent source region highlighted by the Acoustic Analogy, a lot of empirical semi-empirical and RANS-based approaches are available in the literature. Particularly attractive are the RANS-based models that allow a synthesis of the turbulent field throughout the turbulence statistical description of the Reynolds-Averaged Navier-Stokes (RANS) equations.

2.2. Overview of the Thesis

The present dissertation, divided into three main chapters, describes the theoretical and numerical formulation of different alternative computational aeroacoustic methods and their application to typical aeronautics low noise design problems.
In particular, Chapter 3 deals with the theoretical bases of the Acoustic Analogy and the derivation of the convected wave equation in uniform mean flow.

Chapter 4 deals with the development of a Boundary Element method (BEM) for the convected Helmholtz equation. The numerical discretization issues, the implemented boundary conditions and the analytical test cases are also illustrated.

Chapter 5 introduces broadband noise and the statistical models for the source field characterization. In particular, the use of RANS-based methods are finally presented and investigated by using both FEM and BEM approaches.

Finally, Chapter 6 applies the developed methods to the low-noise design problem of the Landing Gear.

3. Acoustic Analogy and Wave equations

3.1. Introduction

Aero-acoustics is the field which studies the sound generated by fluids.
Since the fluid dynamics equations are non-linear an exact solution of these equations is not available. Following the Acoustic Analogy approach introduced by Lighthill [2,3], acoustics can be seen as the small perturbation limit of fluid dynamics in which non-linear effects are neglected, whereas, the mechanisms of sound generation, for instance the sound generated by turbulence, are revised as a source term of a classical acoustic equation.

3.2. The governing equations

According to the continuum hypotheses used in fluid dynamics, fluid motion is described by using the laws of mass, momentum and energy conservation applied to an elementary fluid particle [5]. Applying these laws to an infinitesimal volume element the mass and momentum and energy conservation equations in differential form are achieved. The mass and momentum equations can be written as:

$$\frac{\partial \rho}{\partial t} + \boldsymbol{\nabla} \cdot (\rho \boldsymbol{v}) = m \tag{3.1}$$

$$\frac{\partial}{\partial t}(\rho \boldsymbol{v}) + \boldsymbol{\nabla} \cdot (\boldsymbol{P} + \rho \boldsymbol{v}\boldsymbol{v}) = \boldsymbol{f} \tag{3.2}$$

where, ρ is the fluid density, $\boldsymbol{v}$ is the flow velocity, m the mass source term, $\boldsymbol{f}$ an external force density (like the gravitational force) and $\boldsymbol{P}$ denotes the fluid stress tensor.

The fluid stress tensor is related to the pressure p and the viscous stress tensor $\boldsymbol{\tau}$ by the relationship:

$$\boldsymbol{P} = p\boldsymbol{I} - \boldsymbol{\tau} \tag{3.3}$$

where, $\boldsymbol{I}$ is the unit tensor.

In general, a relationship between $\boldsymbol{\tau}$ and the deformation rate of the fluid element, expressed in the rate-of-strain tensor $\nabla \boldsymbol{v} + (\nabla \boldsymbol{v})^{\mathrm{T}}$ exists . When this relation is linear the fluid is described as Newtonian and the resulting momentum conservation equation is referred to as the Navier-Stokes equation. Even applying a drastic simplification, for compressible fluids as considered in acoustics, the equations still remain quite complicated. A considerable simplification is obtained when the Stokes' hypothesis is assumed, that the fluid is in local thermodynamic equilibrium, so that the pressure p and the thermodynamic pressure are equivalent. In this case:

$$\boldsymbol{\tau} = \mu[\boldsymbol{\nabla v} + (\boldsymbol{\nabla v})^{\boldsymbol{T}}] - \frac{2}{3}\mu(\boldsymbol{\nabla} \cdot \boldsymbol{v})\boldsymbol{I} \tag{3.4}$$

where μ is the dynamic viscosity, in general dependent on the temperature T and the pressure p. and the equation (3.4) represents the constitutive equation.
For m = 0, the energy conservation law is given by:

$$\begin{gathered} \frac{\partial}{\partial t}\rho\left(e + \frac{1}{2}v^2\right) + \boldsymbol{\nabla} \cdot \left(\rho \boldsymbol{v}\left(e + \frac{1}{2}v^2\right)\right) = \\ -\boldsymbol{\nabla} \cdot \boldsymbol{q} - \boldsymbol{\nabla} \cdot (p\boldsymbol{v}) + \boldsymbol{\nabla} \cdot (\boldsymbol{\tau} \cdot \boldsymbol{v}) + \boldsymbol{f} \cdot \boldsymbol{v} \end{gathered} \tag{3.5}$$

where $v = |\boldsymbol{v}|$, e is the internal energy per unit of mass and $\boldsymbol{q}$ is the heat flux due to heat conduction. Adopting the Fourier's law as linear constitutive equation for $\boldsymbol{q}$:

$$\boldsymbol{q} = -K\boldsymbol{\nabla}T \tag{3.6}$$

where K is the heat conductivity which depends on the pressure p and temperature T. Using the fundamental law of thermodynamics for a reversible process:

$$Tds = de + pd(1/\rho) \tag{3.7}$$

and the equation for mechanical energy, obtained by taking the inner product of the momentum conservation law (3.2) with $\boldsymbol{v}$, we obtain the equation for the entropy:

$$\rho T\left(\frac{\partial s}{\partial t}+\boldsymbol{v}\cdot\boldsymbol{\nabla}s\right)=-\boldsymbol{\nabla}\cdot\boldsymbol{q}+\boldsymbol{\tau}:\boldsymbol{\nabla}\boldsymbol{v} \tag{3.8}$$

where:

$$\boldsymbol{\tau}:\boldsymbol{\nabla}\boldsymbol{v}=\boldsymbol{\nabla}\cdot(\boldsymbol{\tau}\cdot\boldsymbol{v})-\boldsymbol{v}\cdot(\boldsymbol{\nabla}\cdot\boldsymbol{\tau}) \tag{3.9}$$

and s is the specific entropy or entropy per unit of mass. When heat conduction $\nabla\cdot\boldsymbol{q}$ and viscous dissipation $\boldsymbol{\tau}:\nabla\boldsymbol{v}$ may be neglected, the flow is *isentropic* (*adiabiatic and reversible*). This means that the entropy s of a fluid particle remains constant:

$$\frac{\partial s}{\partial t}+\boldsymbol{v}\cdot\boldsymbol{\nabla}s=0 \tag{3.10}$$

Equations (3.1)-(3.10) still contain more unknowns than equations. As a closure condition, let's introduce an additional constitutive equation, for example $e = e(\rho, s)$, which implies with equation (3.7):

$$\begin{aligned} p&=\rho^2\left(\frac{\partial e}{\partial\rho}\right)_s \\ T&=\left(\frac{\partial e}{\partial s}\right)_\rho \end{aligned} \tag{3.11}$$

In many cases we will specify an equation of state $p = p(\rho, s)$ rather than $e = e(\rho, s)$. In differential form this becomes:

$$dp=c^2d\rho+\left(\frac{\partial p}{\partial s}\right)_\rho ds \tag{3.12}$$

where $c^2 = \left(\frac{\partial p}{\partial \rho}\right)_s$ is the square of the isentropic speed of sound *c*.

When the same equation of state *c(ρ, s)* is valid for the entire flow, fluid is said *homogeneous*. When the density depends only on the pressure fluid is said *barotropic*. When the fluid is homogeneous and the entropy uniform (d*s* = 0) flow is said *homentropic*.

The heat capacity at constant volume c_V is defined for a reversible process by:

$$c_V = \left(\frac{\partial e}{\partial T}\right)_V \tag{3.13}$$

For an *ideal* gas the energy *e* is a function of the temperature only:

$$e(T) = \int_0^T c_V dT \tag{3.14}$$

For an ideal gas with constant thermal properties we will often use the simplified relation:

$$e = c_V T \tag{3.15}$$

That represents the equation of a *perfect gas*.

3.3. **Governing equation linearization and wave equations**

Starting from the conservation laws and the constitutive equations it is possible to obtain after linearization a wave equation.

Sound is a small perturbation of a steady state pressure, p'/p_0, which propagates as a wave and which is detectable by the human ear. In the acoustic phenomena also the density fluctuations ρ'/ρ_0 and the fluid velocity fluctuation $\boldsymbol{v}'$ associated with the wave propagation, are small. This justifies the use of a linear approximation of the governing equations.

Even with the additional assumption that the flow is frictionless, the resulting equations may still be complex if it is assumed a non-uniform mean flow or a non uniform density distribution ρ_0. A derivation of more general linearized wave equations is illustrated by Goldstein [6] and Pierce [7].

Consider the case of acoustic perturbations (p', ρ', s', $\boldsymbol{v}'$. . .) of a stagnant ($u_0 = 0$) and uniform fluid (p_0, ρ_0, s_0, . . .). In this condition the equations simplify to:

$$\begin{aligned} \frac{\partial \rho'}{\partial t} + \rho_0 \boldsymbol{\nabla} \cdot \boldsymbol{v}' &= 0 \\ \rho_0 \frac{\partial \boldsymbol{v}'}{\partial t} + \boldsymbol{\nabla} p' &= \mathbf{0} \\ \frac{\partial s'}{\partial t} &= 0 \end{aligned} \qquad \textbf{(3.16)}$$

where second order terms in the perturbations have been neglected. The constitutive equation $c^2 = \left(\frac{\partial p}{\partial \rho}\right)_s$ becomes:

$$p' = c_0^2 \rho' \qquad \textbf{(3.17)}$$

By subtracting the time derivative of the mass conservation law from the divergence of the momentum conservation law is possible to eliminate $\boldsymbol{v}$' to obtain the ***wave equation for stagnant flow***:

$$\frac{\partial^2 \rho'}{\partial t^2} - \nabla^2 p' = 0 \tag{3.18}$$

Using the constitutive equation $p' = c_0^2 \rho'$ leads to the wave equations:

$$\begin{aligned} \frac{\partial^2 p'}{\partial t^2} - c_0^2 \nabla^2 p' = 0 \\ \frac{\partial^2 \rho'}{\partial t^2} - c_0^2 \nabla^2 \rho' = 0 \end{aligned} \tag{3.19}$$

In the presence of a mean flow that satisfies the following equations:

$$\begin{aligned} \boldsymbol{\nabla} \cdot \rho_0 \boldsymbol{v_0} = 0 \\ \rho_0 \boldsymbol{v_0} \cdot \boldsymbol{\nabla} \boldsymbol{v_0} = -\boldsymbol{\nabla} p_0 \\ \boldsymbol{v_0} \cdot \boldsymbol{\nabla} s_0 = 0 \\ \boldsymbol{v_0} \cdot \boldsymbol{\nabla} p_0 = c_0^2 \boldsymbol{v_0} \cdot \boldsymbol{\nabla} \rho_0 \end{aligned} \tag{3.20}$$

the linearized conservation laws, and constitutive equation for isentropic flow, become (without sources):

$$\begin{aligned} \frac{\partial \rho'}{\partial t} + \boldsymbol{v_0} \cdot \boldsymbol{\nabla} \rho' + \boldsymbol{v'} \cdot \boldsymbol{\nabla} \rho_0 + \rho_0 \boldsymbol{\nabla} \cdot \boldsymbol{v'} + \rho' \boldsymbol{\nabla} \cdot \boldsymbol{v_0} = 0 \\ \rho_0 \left(\frac{\partial \boldsymbol{v'}}{\partial t} + \boldsymbol{v_0} \cdot \boldsymbol{\nabla} \boldsymbol{v'} + \boldsymbol{v'} \cdot \boldsymbol{\nabla} \boldsymbol{v_0} \right) + \rho' \boldsymbol{v_0} \cdot \boldsymbol{\nabla} \boldsymbol{v_0} = -\boldsymbol{\nabla} p' \\ \frac{\partial s'}{\partial t} + \boldsymbol{v_0} \cdot \boldsymbol{\nabla} s' + \boldsymbol{v'} \cdot \boldsymbol{\nabla} s_0 = 0 \\ \frac{\partial p'}{\partial t} + \boldsymbol{v_0} \cdot \boldsymbol{\nabla} p' + \boldsymbol{v'} \cdot \boldsymbol{\nabla} p_0 = c_0^2 \left(\frac{\partial \rho'}{\partial t} + \boldsymbol{v_0} \cdot \boldsymbol{\nabla} \rho' + \boldsymbol{v'} \cdot \boldsymbol{\nabla} \rho_0 \right) \\ + c_0^2 (\boldsymbol{v_0} \cdot \boldsymbol{\nabla} \rho_0) \left(\frac{p'}{p_0} - \frac{\rho'}{\rho_0} \right) \end{aligned} \tag{3.21}$$

A wave equation can be obtained from these equations if simplifying assumptions are introduced. For a uniform medium with uniform flow velocity we obtain the ***convected wave equation for uniform mean flow***:

$$(\frac{\partial}{\partial t} + \boldsymbol{v_0} \cdot \boldsymbol{\nabla})^2 p' - c_0^2 \nabla^2 p' = 0 \quad \textbf{(3.22)}$$

Where the $\frac{\partial}{\partial t} + \boldsymbol{v_0} \cdot \boldsymbol{\nabla}$ denotes the Lagrangian derivative.

3.4. Lighthill's analogy

Lighthill [2,3] derived from the exact equations of motion a non-homogeneous wave equation with the propagation term at the left-hand-side.
Starting from the time derivative of the continuity equation and subtracting the divergence of the momentum equation, assuming the absence of external forces and mass sources, Lighthill achieved:

$$\frac{\partial^2 \rho'}{\partial t^2} - c_0^2 \frac{\partial^2 \rho'}{\partial x_i^2} = \frac{\partial^2 T_{ij}}{\partial x_i \partial x_j} \quad \textbf{(3.23)}$$

where the Lightill's stress tensor T_{ij} is defined by:

$$T_{ij} = \rho v_i v_j - \tau_{ij} + (p' - c_0^2 \rho')\delta_{ij} \quad \textbf{(3.24)}$$

In T_{ij} equation three basic aero-acoustic processes can be distinguished, which result in sources of sound:

- *the non-linear convective forces described by the Reynolds stress tensor* $\rho v_i v_j$,
- *the viscous forces* τ_{ij},
- *the deviation from a uniform sound velocity* c_0 *or the deviation from an isentropic behavior* $p' - c_0^2 \rho'$.

Without approximations, equation (3.23) is exact and it is not easier to solve than the original equations of motion, since the right hand side contains the acoustic field and cannot be solved as a wave equation in explicit way by means of Green's function technique.

However, the analogy is not complete unless the following conditions are met:

- *T_{ij} = 0 in the region where the sound is to be predicted (the postulated fictitious acoustic medium is identical to a region of the real flow where c_0 is constant and there is no mean flow).*
- *Exist a way to compute T_{ij} indipendently of the left hand side of the equation.*

Lighthill proposed some simplifications:

- At high Reynolds numbers, viscous effect $\tau_{ij}$are much smaller than inertial effects, so the viscous stress tensor can be neglected when compared to the Reynolds stresses $\rho v_i v_j$.
- The assumption of isentropic flow $p' - c_0^2 \rho' = 0$
- The hypothesis of low Mach number ensures that the flow can be assumed incompressible.

In the hypotheses before mentioned, Lighthill's tensor reads:

$$T_{ij} = \rho_0 U_i U_j \tag{3.25}$$

where ***U*** is the mean velocity field.
This represents an incompressible approximation of the real flow and can be used as a forcing term for the acoustic wave equation that can be solved with the Green's function technique. It is important to highlight that under the Lighthill hypotheses the density based equation (3.23) is equivalent to the pressure based equation that reads:

$$\frac{1}{c_0^2}\frac{\partial^2 p'}{\partial t^2} - \frac{\partial^2 p'}{\partial x_i^2} = \frac{\partial^2 T_{ij}}{\partial x_i \partial x_j} \tag{3.26}$$

T_{ij} could be determined experimentally or from direct numerical solutions of the Navier-Stokes equations or from semi-empirical or stochastic source models.

It is trivial to show that convective Lighthill's equation assumes the same form of the equation (3.26) [8]. Considering the linearized Lagrangian derivative $\frac{D}{Dt} = \frac{\partial}{\partial t} + \boldsymbol{v_0} \cdot \boldsymbol{\nabla}$, the convective equation reads:

$$\frac{1}{c_0^2}\frac{D^2 p'}{Dt^2} - \frac{\partial^2 p'}{\partial x_i^2} = \frac{\partial^2 T_{ij}}{\partial x_i \partial x_j} \tag{3.27}$$

3.5. Green's Functions of the standard and convected Wave Equations

The acoustic analogy has the formal advantage of formulating the complicated problem of the noise generation and radiation in the more standard problem of the inhomogeneous wave equation. Indeed, assuming that the source terms are previously determined, the solution is given by the Green's function approach.

Consider the standard wave equation of the Lighthill's equation (3.26). The Green's function $g(\boldsymbol{x}|t;\boldsymbol{x_q}|\tau)$ at the point $\boldsymbol{x}$ and time t, produced by the source at point $\boldsymbol{x_q}$ and time τ, is the pulse response satisfying:

$$-\frac{1}{c_0^2}\frac{\partial^2 g}{\partial t^2} + \frac{\partial^2 g}{\partial x_i^2} = -\delta(\boldsymbol{x} - \boldsymbol{x_q})\delta(t - \tau) \tag{3.28}$$

With application of the Fourier transform to the standard wave equation, the frequency counterpart under the $-i\omega t$ convention reads:

$$k^2 p + \nabla^2 p = 0 \tag{3.29}$$

where it is tacit that the new variables are defined in the Fourier domain.

Equation (3.29) represents the homogeneous Helmholtz equation and k is the wave number defined as ω/c_0. The pulse response of the Helmholtz equation reads:

$$k^2 g + \nabla^2 g = -\delta(\boldsymbol{x} - \boldsymbol{x_q}) \tag{3.30}$$

In the case of its inhomogeneous counterpart, a given space-dependent function is applied on the right hand side (RHS). In the simplest case of an harmonic point source A, the wave equation leads to the inhomogeneous Helmholtz equation:

$$k^2 p + \nabla^2 p = -A\delta(\boldsymbol{x} - \boldsymbol{x_q}) \tag{3.31}$$

The wave solution of the inhomogeneous equation is provided by the product between the source term and the Green's function of the homogeneous equation.
In the general case of multiple point source terms, the wave solution reads:

$$p(\boldsymbol{x}) = \int \; g(\boldsymbol{x}, \boldsymbol{x_q}) A(\boldsymbol{x_q}) d\boldsymbol{x_q} \tag{3.32}$$

The analytical solution of the Green function in free-field conditions, $g(\boldsymbol{x}, \boldsymbol{x_q})$, reads [9]:

$$\begin{cases} g(\boldsymbol{x}, \boldsymbol{x_q}) = \dfrac{i}{4} H_0^1[kr] & 2D \\ g(\boldsymbol{x}, \boldsymbol{x_q}) = \dfrac{1}{4\pi r} e^{ikr} & 3D \end{cases} \tag{3.33}$$

where r is the source-observer distance and H_0^1 is the Henkel function of the first kind and order zero.

In the case of the convected wave equation (3.22), the frequency counterpart under the $-i\omega t$ can be expressed as:

$$(-\mathrm{ik} + \mathbf{M} \cdot \boldsymbol{\nabla})^2 p - \nabla^2 p = 0 \tag{3.34}$$

Whereas, the pulse response of the Helmholtz equation reads:

$$(-\mathrm{ik} + \mathbf{M} \cdot \boldsymbol{\nabla})^2 g - \nabla^2 g = \delta(\boldsymbol{x} - \boldsymbol{x_q}) \tag{3.35}$$

where $\boldsymbol{M}$ is the Mach number of the mean flow field.

The analytical solution of the Green function in free-field conditions $g(\boldsymbol{x}, \boldsymbol{x_q})$ reads [9]:

$$\begin{cases} g(\boldsymbol{x}, \boldsymbol{x_q}) = \dfrac{i\gamma}{4}\exp(-ik\gamma^2 \boldsymbol{M}\cdot(\boldsymbol{x}-\boldsymbol{x_q}))H_0^1[k\gamma R_M] \quad 2D \\ g(\boldsymbol{x}, \boldsymbol{x_q}) = \gamma\exp\left(-ik\gamma^2 \boldsymbol{M}\cdot(\boldsymbol{x}-\boldsymbol{x_q})\right)\dfrac{1}{4\pi R_M}e^{ik\gamma R_M} \quad 3D \\ R_M = \sqrt{\gamma^2\left((\boldsymbol{x}-\boldsymbol{x_q})^T\cdot\boldsymbol{M}\right)^2 + (\boldsymbol{x}-\boldsymbol{x_q})^T\cdot(\boldsymbol{x}-\boldsymbol{x_q})} \end{cases} \tag{3.36}$$

The Green function gradient can be expressed as a function of the Green function and the vector operator $\boldsymbol{F}(\boldsymbol{x}, \boldsymbol{x_q})$, that assumes a different form for the 2D and 3D cases:

$$\begin{cases} \nabla g(\boldsymbol{x}, \boldsymbol{x_q}) = g(\boldsymbol{x}, \boldsymbol{x_q})\boldsymbol{F}(\boldsymbol{x}, \boldsymbol{x_q}) \\ \boldsymbol{F}_{2D}(\boldsymbol{x}, \boldsymbol{x_q}) = ik\gamma^2\boldsymbol{M} + k\gamma\dfrac{H_1^1[k\gamma R_M]}{H_0^1[k\gamma R_M]}\dfrac{1}{R_M}\left(\gamma^2\left[\boldsymbol{M}\cdot(\boldsymbol{x}-\boldsymbol{x_q})\boldsymbol{M}\right] + (\boldsymbol{x}-\boldsymbol{x_q})\right) \\ F_{3D}(\boldsymbol{x}, \boldsymbol{x_q}) = ik\gamma[\nabla R_M + \gamma\boldsymbol{M}] - \dfrac{1}{R_M}\nabla R_M \end{cases} \tag{3.37}$$

where ∇R_M is computed as:

$$\begin{aligned} \frac{\partial R_M}{\partial x_{q,i}} = \frac{1}{R_M}\{&-(\gamma^2 M_i^2 + 1)(x_i - x_{q,i}) - \gamma^2 M_i M_{i+1}(x_{i+1} \\ &- x_{q,i+1}) - \gamma^2 M_i M_{i-1}(x_{i-1} - x_{q,i-1})\} \end{aligned} \tag{3.38}$$

4. The Boundary Element Method for the Convected Wave Equation

4.1. Introduction

According to the Acoustic Analogy an alternative to LES or DES simulation for noise prediction consists of separating the noise radiation and noise generation problems. The noise radiation and the body scattering are dealt with acoustic equations whereas the noise generation problem is treated separately.

Numerical approaches such as the Finite Element Method (FEM) and the Boundary Element Method (BEM) allow acoustic simulations accounting for scattering from arbitrary bodies [8,9,10,11].

This Chapter deals with a BEM method applied to the convected Helmholtz equation. The Boundary Element Method (BEM) is based on an application of the divergence theorem to the governing equations (Paragraph 4.2). This approach allows leading back the solution of a volume problem to the body surface one exploiting the collocation approach (Paragraph 4.3).
After the solution on the surface is achieved with the collocation approach, the acoustic pressure can be easily predicted for any observer in the volume.
A set of BEM boundary conditions (Paragraph 4.4) are implemented in a generic form and fill up the final BEM system matrix disjointed from the governing equations (Paragraphs 4.5). The CHIEF method is also implemented for external flow problems stability (Paragraphs 4.6). Finally the validation against internal and external test cases available in literature is presented (Paragraphs 4.8).

4.2. **Boundary Integral Equations**

Consider the Green function of the convected wave equation:

$$(-\mathrm{ik} + \mathbf{M}\cdot\boldsymbol{\nabla})^2 G(\boldsymbol{x}|\boldsymbol{x_q}) - \nabla^2 G(\boldsymbol{x}|\boldsymbol{x_q}) = \delta(\boldsymbol{x}-\boldsymbol{x_q}) \tag{4.1}$$

and the corresponding equation for the free-space conjugated Green's function $g^*(\boldsymbol{x}|\boldsymbol{x_O})$, which satisfies:

$$(-\mathrm{ik} - \mathbf{M}\cdot\boldsymbol{\nabla})^2 g^*(\boldsymbol{x}|\boldsymbol{x_O}) - \nabla^2 g^*(\boldsymbol{x}|\boldsymbol{x_O}) = \delta(\boldsymbol{x}-\boldsymbol{x_O}) \tag{4.2}$$

the difference between the product of $g^*$with equation (4.1) and the product of G with equation (4.2) leads to:

$$\begin{gathered} g^*[k^2 + (\mathbf{M}\cdot\boldsymbol{\nabla})^2 - 2ik(\mathbf{M}\cdot\boldsymbol{\nabla}) - \nabla^2]G \\ -G[k^2 + (\mathbf{M}\cdot\boldsymbol{\nabla})^2 + 2ik(\mathbf{M}\cdot\boldsymbol{\nabla}) - \nabla^2]g^* \\ = g^*(\boldsymbol{x}|\boldsymbol{x_O})\delta(\boldsymbol{x}-\boldsymbol{x_q}) - G(\boldsymbol{x}|\boldsymbol{x_q})\delta(\boldsymbol{x}-\boldsymbol{x_O}) \end{gathered} \tag{4.3}$$

$$\begin{gathered} -2ik[g^*(\mathbf{M}\cdot\boldsymbol{\nabla})G + G(\mathbf{M}\cdot\boldsymbol{\nabla})g^*] \\ + [g^*(\mathbf{M}\cdot\boldsymbol{\nabla})^2 G - G(\mathbf{M}\cdot\boldsymbol{\nabla})^2 g^*] \\ + [G\nabla^2 g^* - g^*\nabla^2 G] \\ = g^*(\boldsymbol{x}|\boldsymbol{x_O})\delta(\boldsymbol{x}-\boldsymbol{x_q}) - G(\boldsymbol{x}|\boldsymbol{x_q})\delta(\boldsymbol{x}-\boldsymbol{x_O}) \end{gathered} \tag{4.4}$$

by introducing a vector operator $\boldsymbol{P}$, the equation can be expressed in form of the divergence of $\boldsymbol{P}$

$$\begin{gathered} \boldsymbol{\nabla}\cdot\boldsymbol{P}(G, g^*) \\ =\boldsymbol{\nabla}\cdot\{-2ik(\mathbf{M}g^*G) + [\mathbf{M}(g^*\boldsymbol{\nabla}G - G\boldsymbol{\nabla}g^*)\cdot\mathbf{M}] + [G\nabla^2 g^* - g^*\nabla^2 G]\} \\ = g^*(\boldsymbol{x}|\boldsymbol{x_O})\delta(\boldsymbol{x}-\boldsymbol{x_q}) - G(\boldsymbol{x}|\boldsymbol{x_q})\delta(\boldsymbol{x}-\boldsymbol{x_O}) \end{gathered} \tag{4.5}$$

Applying the integral over the entire volume *V* on both sides of equation (4.5), it is allowed to make use of the divergence theorem and the general point $\boldsymbol{x}$ reduces to the general surface point $\boldsymbol{x_s}$, whereas, the volume integral reduces to the surface integral:

$$\begin{aligned} \iiint_{\mathcal{V}(\boldsymbol{x})} \boldsymbol{\nabla}\cdot\boldsymbol{P}(G,g^*)d\mathcal{V} &= \oiint_{\mathcal{S}(\boldsymbol{x^s})} \boldsymbol{P}(G,g^*)(-\boldsymbol{n})d\mathcal{S} \\ = \iiint_{\mathcal{V}(\boldsymbol{x})} g^*(\boldsymbol{x}|\boldsymbol{x_O})\delta(\boldsymbol{x}-\boldsymbol{x_q})d\mathcal{V} &- \iiint_{\mathcal{V}(\boldsymbol{x})} G(\boldsymbol{x}|\boldsymbol{x_q})\delta(\boldsymbol{x}-\boldsymbol{x_O})d\mathcal{V} \\ = g^*(\boldsymbol{x_q}|\boldsymbol{x_O}) &- CG(\boldsymbol{x_O}|\boldsymbol{x_q}) \end{aligned} \tag{4.6}$$

where the evaluation of the right hand side $g^*(\boldsymbol{x_q}|\boldsymbol{x_O}) - CG(\boldsymbol{x_O}|\boldsymbol{x_q})$ is achieved from the general property of the Dirac delta function $\iiint_{\mathcal{V}(\boldsymbol{x})} h(\boldsymbol{x})\delta(\boldsymbol{x}-\boldsymbol{x_q})d\mathcal{V} = h(\boldsymbol{x_q})$.

The divergence theorem uses normal unitary vectors pointing outwards from the fluid volume. Assuming that in the BEM code the normal unitary vectors are pointing inwards into the fluid volume, the normal unitary vector $\boldsymbol{n}$ in the equation (4.6) requires to be multiplied by the factor −1.

The coefficient *C* allows accounting for different point location, *C=0*, for points outside the flow, *C=1*, for points inside the flow and *C=1/2* for points in the surface boundaries.

Indicating the general point $\mathbf{x_O}$ as $\boldsymbol{x}$ and exploiting the reciprocity theorem, for which $g^*(x_q|x_O) = g(x_O|x_q)$, the Boundary Integral Equation reads:

$$CG(\boldsymbol{x}|\boldsymbol{x_q}) = g(\boldsymbol{x}|\boldsymbol{x_q}) + \oint_{\mathcal{S}(\boldsymbol{x^s})} \boldsymbol{P}\left(G(\boldsymbol{x^s}|\boldsymbol{x_q}), g(\boldsymbol{x}|\boldsymbol{x^s})\right)\cdot\boldsymbol{n}d\mathcal{S} \tag{4.7}$$

where the left hand side, $G(\boldsymbol{x}|\boldsymbol{x_q})$, represents the total acoustic pressure whereas the right hand side represents the sum of a spherical incident wave, $g(\boldsymbol{x}|\boldsymbol{x_q})$, and the scattered one ($\oint_{\mathcal{S}(\boldsymbol{x^s})} \boldsymbol{P}\left(G(\boldsymbol{x^s}|\boldsymbol{x_q}), g(\boldsymbol{x}|\boldsymbol{x^s})\right)\cdot\boldsymbol{n}d\mathcal{S}$).

Introducing the local coordinates system (***t, s, n***) where ***t*** and ***s*** represent the tangential plane to the surface and ***n*** is the normal pointing away to the surface, the inner products can be expressed as:

$$\begin{gathered}\boldsymbol{\nabla} G \cdot \boldsymbol{M} = \boldsymbol{M} \cdot \boldsymbol{\nabla} G = M_t \frac{\partial G}{\partial t} + M_s \frac{\partial G}{\partial s} + M_n \frac{\partial G}{\partial n} \\ \boldsymbol{\nabla} G \cdot \boldsymbol{t} = \frac{\partial G}{\partial t},\ \boldsymbol{\nabla} G \cdot \boldsymbol{s} = \frac{\partial G}{\partial s},\ \boldsymbol{\nabla} G \cdot \boldsymbol{n} = \frac{\partial G}{\partial n} \\ \mathbf{M} \cdot \boldsymbol{t} = M_t,\ \mathbf{M} \cdot \boldsymbol{s} = M_s,\ \mathbf{M} \cdot \boldsymbol{n} = M_n \\ \boldsymbol{\nabla_{tg}} = \left(\frac{\partial}{\partial t}, \frac{\partial}{\partial s}\right),\ \mathbf{M_{tg}} = (M_t, M_s),\end{gathered} \tag{4.8}$$

Solving the inner product $\boldsymbol{P} \cdot \boldsymbol{n}$, and noting that the integral on a closed surface of the divergence of a general vector function ***f,*** $\oint_{S(\boldsymbol{x^s})} \boldsymbol{\nabla_{tg}} \cdot (\boldsymbol{f}) d\mathcal{S}$**,** is zero, the *Boundary Integral Equation* reads:

$$\begin{aligned} C G(\boldsymbol{x}|\boldsymbol{x_q}) = g(\boldsymbol{x}|\boldsymbol{x_q}) &- \oint_{S(\boldsymbol{x^s})} B_1(\boldsymbol{x}|\boldsymbol{x^s}) G(\boldsymbol{x^s}|\boldsymbol{x_q}) d\mathcal{S} \\ &- \oint_{S(\boldsymbol{x^s})} B_2(\boldsymbol{x}|\boldsymbol{x^s}) \frac{\partial G}{\partial n}(\boldsymbol{x^s}|\boldsymbol{x_q}) d\mathcal{S} \end{aligned} \tag{4.9}$$

where the kernel equations, $B_1(\boldsymbol{x}|\boldsymbol{x^s})$ and $B_2(\boldsymbol{x}|\boldsymbol{x^s})$ are expressed as:

$$\begin{gathered} B_1(\boldsymbol{x}|\boldsymbol{x^s}) = \left\{2ikM_n g + [M_n \mathbf{M} - \mathbf{n}] \cdot \boldsymbol{\nabla} g \ + \ \boldsymbol{\nabla_{tg}} \cdot \left[g M_n \mathbf{M_{tg}}\right]\right\} \\ B_2(\boldsymbol{x}|\boldsymbol{x^s}) = (1 - M_n^2) g \end{gathered} \tag{4.10}$$

and where the $\boldsymbol{\nabla_{tg}} \cdot \left[g M_n \mathbf{M_{tg}}\right]$ term can be explicated as:

$$\boldsymbol{\nabla_{tg}} \cdot \left[g M_n \mathbf{M_{tg}}\right] = M_n \left[M_t \frac{\partial g}{\partial t} + M_s \frac{\partial g}{\partial s}\right] \tag{4.11}$$

4.3. Collocation Approach

The Boundary Integral Equation (4.9) (BIE) underlines that to compute the Green function *G* at any point $\boldsymbol{x}$, the knowledge of the unknowns G and $\frac{\partial G}{\partial n}$ on the body surface is needed.

Since equation (4.9) is valid everywhere in the field, it is possible to compute the equation on the surface assuming the coefficient *C=1/2*. Afterwards, the Green function at a point $\overline{\boldsymbol{x}}^{\boldsymbol{s}}$ on the surface is achieved by:

$$\frac{1}{2}G\left(\overline{\boldsymbol{x}}^{\boldsymbol{s}}\middle|\boldsymbol{x_q}\right) = g\left(\overline{\boldsymbol{x}}^{\boldsymbol{s}}\middle|\boldsymbol{x_q}\right) - \oint_{\mathcal{S}(\boldsymbol{x}^{\boldsymbol{s}})} B_1(\overline{\boldsymbol{x}}^{\boldsymbol{s}}|\boldsymbol{x}^{\boldsymbol{s}})G\left(\boldsymbol{x}^{\boldsymbol{s}}\middle|\boldsymbol{x_q}\right)d\mathcal{S} - \oint_{\mathcal{S}(\boldsymbol{x}^{\boldsymbol{s}})} B_2(\overline{\boldsymbol{x}}^{\boldsymbol{s}}|\boldsymbol{x}^{\boldsymbol{s}})\frac{\partial G}{\partial n}\left(\boldsymbol{x}^{\boldsymbol{s}}\middle|\boldsymbol{x_q}\right)d\mathcal{S} \tag{4.12}$$

Therefore, for a surface discretization of *N* nodes, the BIE leads to *N* equations, one for each node of the surface. Indeed, N equations with *2N* unknowns are achieved (*N* unknowns for G and *N* unknowns for $\frac{\partial G}{\partial n}$). The equation system can be solved introduced new *N* boundary conditions equations expressed as a linear relation between G and $\frac{\partial G}{\partial n}$. The system solution leads to the knowledge of the *2N* unknowns.

4.4. Boundary conditions

All boundary condition are expressed as a relation between the Green function normal derivative $\frac{\partial G}{\partial n}$ and the Green function *G*. The most of all are expressed as local relations, that is the Green function normal derivative at the point $\boldsymbol{x}$, depends only on the Green function at point $\boldsymbol{x}$, as:

$$\alpha\frac{\partial G}{\partial n} + \beta G = \gamma \tag{4.13}$$

More sophisticated boundary condition in which the relation between the Green function normal derivative $\frac{\partial G}{\partial n}$ and the Green function *G* is not local can be taken in

account. An example is the so-called plane-baffle free-field radiation described in [10].

4.4.1. **Impedance Boundary condition for uniform mean flow**

Considering an absorbing material with a given impedance Z applied on a vibrating structure as depicted in Figure 4.1.

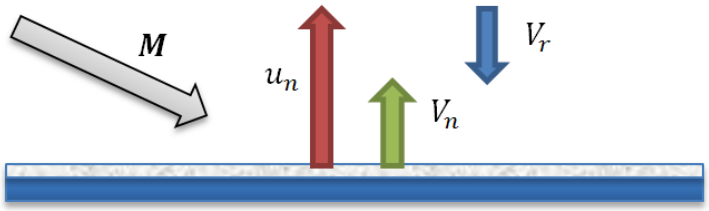

Figure 4.1 – Vibrating surface with absorbing material.

The impedance, Z, is defined via the Fourier transformed signal as the ratio between the pressure and the normal relative velocity V_r, assumed positive pointing into the surface.

$$\mathrm{Z} = \frac{p}{V_r} \tag{4.14}$$

Assuming with u_n the fluid normal velocity at the surface and with V_n the surface normal velocity, both defined positive pointing into the fluid, the impedance equation reads:

$$u_n = -\frac{p}{Z} + V_n \tag{4.15}$$

The linearized momentum equation for *uniform mean flow* can be written as:

$$\rho_0 \left(\frac{\partial \boldsymbol{u}}{\partial t} + \boldsymbol{v_0} \cdot \boldsymbol{\nabla u} \right) = -\boldsymbol{\nabla} p \tag{4.16}$$

Multiplying for the normal vector, $\boldsymbol{n}$, pointing outward the surface and introducing the frequency domain counterpart of the linearized momentum equation with the $-i\omega t$ convention, the momentum equation reads:

$$\rho_0(-i\omega + \boldsymbol{v_0}\cdot\boldsymbol{\nabla})u_n = -\frac{\partial p}{\partial n} \tag{4.17}$$

where ρ_0 and $\boldsymbol{v_0}$ are the mean flow density and velocity.
Substituting the equation (4.15) in the linearized momentum equation (4.17), we achieve the impedance boundary condition for a wall with impedance Z, and a vibrating velocity V_n as it follows:

$$\frac{\partial p}{\partial n} = -ik\frac{1}{\left(\frac{Z}{\rho c} - \boldsymbol{M}\cdot\boldsymbol{n}\right)}p + ik\frac{Z}{\left(\frac{Z}{\rho c} - \boldsymbol{M}\cdot\boldsymbol{n}\right)}V_n \tag{4.18}$$

From the impedance boundary condition it is straightforward to deduce the *Neumann boundary condition* (vibrating wall) for $Z = +\infty$ that reads:

$$\frac{\partial p}{\partial n} = i\rho\omega V_n \tag{4.19}$$

Assuming $V_n = 0$, the Neumann boundary condition leads to the *rigid wall boundary condition* $\frac{\partial p}{\partial n} = 0$.

The impedance boundary condition is derived with the assumption of V_r pointing into the surface and the $-i\omega t$ convention.
If the impedance Z is available under the $i\omega t$ convention, it has to be taken by changing the sign of the imaginary part of the impedance. Whereas, if V_r is assumed positive pointing into the fluid, it has to be taken by changing the sign to all the impedance.

4.4.1. **Dirichlet boundary condition**

A very simple boundary condition is achieved by imposing the acoustic pressure on a boundary surface as $p = p_0$.

4.4.1. **Scattering boundary condition**

Consider the general problem of the acoustic scattering by a rigid body surface described by the convected wave equation as:

$$\begin{cases} (-\mathrm{ik} + \mathbf{M} \cdot \boldsymbol{\nabla})^2 p - \nabla^2 p = 0 \\ \dfrac{\partial p}{\partial n} = 0 \end{cases} \tag{4.20}$$

where p is the total pressure. Denoting with p_i the incident component and with p_s the scattered component, the rigid wall boundary condition leads to:

$$\frac{\partial p_s}{\partial n} = -\frac{\partial p_i}{\partial n} \tag{4.21}$$

Therefore the scattering field can be achieved by solving the following problem for the scattering field where the $\frac{\partial p_i}{\partial n}$ is assumed to be a known variable.

$$\begin{cases} (-\mathrm{ik} + \mathbf{M} \cdot \boldsymbol{\nabla})^2 p_s - \nabla^2 p_s = 0 \\ \dfrac{\partial p_s}{\partial n} = -\dfrac{\partial p_i}{\partial n} \end{cases} \tag{4.22}$$

The total pressure can be finally determined as:

$$p = p_i + p_s \tag{4.23}$$

The decomposition of the acoustic field in the incident and scattered parts allows separating the problem of the free-field noise generation by multipolar sources and the body surface scattering. A typical example is the rotor noise scattering by the helicopter fuselage or the propeller noise scattering by the wing-body and fuselage

[12,13]. The rotor noise is generally computed with free-field integral methods based on the FW-H equation [4,14]. Following the scattering boundary condition approach, the solution of the FW-H equation is seen as the incident field, whereas the scattering field by the fuselage is computed solving the equations (4.22).

4.5. Numerical implementation

Consider a generic body with surface $\mathcal{S}$, discretized with N surface panels $\mathcal{S}_i$, such as $\mathcal{S} = \sum_{i=1}^{N} \mathcal{S}_i$. The application of quadrature rule with a polynomial of degree zero for the integration of the BIE (4.9) leads to:

$$CG(\boldsymbol{x}|\boldsymbol{x_q}) = g(\boldsymbol{x}|\boldsymbol{x_q}) - \sum_{j=1}^{N} B_1(\boldsymbol{x}|\boldsymbol{x_j}) G(\boldsymbol{x_j}|\boldsymbol{x_q}) \mathcal{S}_j - \sum_{j=1}^{N} B_2(\boldsymbol{x}|\boldsymbol{x_j}) \frac{\partial G}{\partial n}(\boldsymbol{x_j}|\boldsymbol{x_q}) \mathcal{S}_j \tag{4.24}$$

where $\boldsymbol{x_j}$ is the centroid of the generic panel of area $\mathcal{S}_j$. Subsequently, the collocation approach for the BIE (4.12) leads to:

$$\frac{1}{2} G(\boldsymbol{x_i}|\boldsymbol{x_q}) = g(\boldsymbol{x_i}|\boldsymbol{x_q}) - \sum_{j=1}^{N} B_1(\boldsymbol{x_i}|\boldsymbol{x_j}) G(\boldsymbol{x_j}|\boldsymbol{x_q}) \mathcal{S}_j - \sum_{j=1}^{N} B_2(\boldsymbol{x_i}|\boldsymbol{x_j}) \frac{\partial G}{\partial n}(\boldsymbol{x_j}|\boldsymbol{x_q}) \mathcal{S}_j \tag{4.25}$$

where $\boldsymbol{x_i}$ is the centroid of the panel for which the BIE solution is looked for.

$$\frac{1}{2} G(\boldsymbol{x_i}|\boldsymbol{x_q}) = g(\boldsymbol{x_i}|\boldsymbol{x_q}) - \sum_{j=1}^{N} B_1(\boldsymbol{x_i}|\boldsymbol{x_j}) G(\boldsymbol{x_j}|\boldsymbol{x_q}) \mathcal{S}_j - \sum_{j=1}^{N} B_2(\boldsymbol{x_i}|\boldsymbol{x_j}) \frac{\partial G}{\partial n}(\boldsymbol{x_j}|\boldsymbol{x_q}) \mathcal{S}_j \tag{4.26}$$

and the generic boundary condition (4.13) leads to:

$$\alpha(\boldsymbol{x_i})\frac{\partial G}{\partial n}(\boldsymbol{x_i}|\boldsymbol{x_q}) + \beta(\boldsymbol{x_i})G(\boldsymbol{x_i}|\boldsymbol{x_q}) = \gamma(\boldsymbol{x_i}) \tag{4.27}$$

The discretization provides a linear system with *2N* equations and *2N* unknown. Thus, the matrix of the Boundary Element (BEM) problem assumes the following form:

$$\begin{bmatrix} \frac{1}{2}\bar{\bar{I}} + \bar{\bar{B}}_1 & \bar{\bar{B}}_2 \\ \bar{\bar{\beta}} & \bar{\bar{\alpha}} \end{bmatrix} \begin{Bmatrix} \bar{G} \\ \frac{\partial \bar{G}}{\partial n} \end{Bmatrix} = \begin{Bmatrix} \bar{g} \\ \bar{\gamma} \end{Bmatrix} \tag{4.28}$$

Or in compact form $\boldsymbol{B}(\omega) \cdot \boldsymbol{G}(\omega, \boldsymbol{x_q}) = \boldsymbol{g}(\omega, \boldsymbol{x_q})$ where **G** is the unknowns vector and ω is the angular frequency.

In the equation (4.28) $\bar{\bar{I}}(NXN)$ represents the identity matrix, $\bar{\bar{B}}_1(NXN)$ and $\bar{\bar{B}}_2(NXN)$ contain the $B_1(\boldsymbol{x_i}|\boldsymbol{x_j})$ and the $B_2(\boldsymbol{x_i}|\boldsymbol{x_j})$ coefficients and the $\bar{\bar{\beta}}(NXN)$ and $\bar{\bar{\alpha}}(NXN)$ are the diagonal matrixes containing the $\beta(\boldsymbol{x_i})$ and $\alpha(\boldsymbol{x_i})$ coefficients.

The integrands $B_1$and B_2 contain the free-field Green functions that are singular for $\boldsymbol{x_i} = \boldsymbol{x_j}$**,** leading to singular values of B_1 and B_2.
These singularities don't prevent the integral evaluation that is not singular. In order to evaluate numerically the integrals of the equation (4.26), the surface panels corresponding to the diagonal elements of the matrix are subdivided in three sub-elements**.** For the linear property, the integral is evaluated as the sum of the integrals of each sub-element. The integrands $B_1$and B_2 of each sub-element are computed respect to the centroid of the master element according to:

$$\begin{aligned} B_1(\boldsymbol{x_i}|\boldsymbol{x_i})\mathcal{S}_i &= \sum_{h=1}^{3} B_1(\boldsymbol{x_i}|\boldsymbol{x_h})\mathcal{S}_h \\ B_2(\boldsymbol{x_i}|\boldsymbol{x_i})\mathcal{S}_i &= \sum_{h=1}^{3} B_2(\boldsymbol{x_i}|\boldsymbol{x_h})\mathcal{S}_h \end{aligned} \tag{4.29}$$

where $\mathcal{S}_i = \sum_{h=1}^{3} \mathcal{S}_h$.

Once the system (4.28) is solved for each angular frequency and source point of interest, the Green function $G(\boldsymbol{x}|\boldsymbol{x_q})$, for each observer, $\boldsymbol{x}$, and source point, $\boldsymbol{x_q}$, can be achieved by means the equation (4.9).

4.6. CHIEF method

A typical problem of the BEM approaches for external problems is the non-uniqueness that appears for some specific frequency values. For these frequencies, corresponding to some eigenfrequencies of the interior problem, the Helmholtz equation admits two solutions. This aspect produces, from a numerical point of view, an indetermination in the numerical system solution around these frequencies.
The adopted strategy is a variant of the CHIEF method [15,16,17] proposed by [10]. It consists in the introduction of N_{chief} equations in the system corresponding to N_{chief} internal points. These internal points are collocated with a random procedure and the number N_{chief} is achieved as a fraction of the total number of the points. A value of *5%-10%* of the total number of points is considered adequate.
For the internal points, the equation (4.24) is applied by using the coefficient *C=0* and the new equations system leads to:

$$\begin{bmatrix} \frac{1}{2}\bar{\bar{I}} + \bar{\bar{B}}_1 & \bar{\bar{B}}_2 \\ \bar{\bar{B}}_1{}^{c} & \bar{\bar{0}} \\ \bar{\bar{\beta}} & \bar{\bar{\alpha}} \end{bmatrix} \begin{Bmatrix} \bar{G} \\ \frac{\partial \bar{G}}{\partial n} \end{Bmatrix} = \begin{Bmatrix} \bar{g} \\ \bar{0} \\ \bar{\gamma} \end{Bmatrix} \tag{4.30}$$

Where the kernel $\bar{\bar{B}}_1{}^{c}$ is evaluated at the CHIEF internal points. The new system matrix has dimension $\left[\left(2N + N_{chief}\right)X2N\right]$ and requires to be solved with a least-square technique.

4.7. Numerical aspects

The BEM approach has been implemented in order to manage hybrid unstructured grids treating segment, triangular and quadrilateral elements.

The normal vector direction of each element (Eq. (4.10)) is managed with a semi-automatic procedure only for single-connected domains by specifying an internal point of the domain and the type of simulation (internal or external problem) to be performed. However, for multi-connected domains a post-processing file is generated for checking the right direction of the normal vectors.

The BEM approach builds up the global system matrix by assembling different matrix blocks for the governing equations and the boundary conditions (Eq. (4.30)). This strategy allows a more general and efficient implementation of the boundary conditions.

The CHIEF kernel generates in a random way the needed internal points according the procedure described in Paragraph 4.6, once the user has previously defined bounding boxes where collocate the points.

As viewed in Paragraph 4.5, BEM leads to a dense system matrix. This implies that computational time and memory increase quadratically with the number of elements which limiting the use of the BEM of large-scale simulations. Many methods have been developed to reduce the size of the system matrix: the most known and efficient is the Fast Multipole Method (FMM) [18,19,20]. The implementation of these methods is not the objective of this work.

4.8. Validation test cases

The BEM code has been tested with two-dimensional and three-dimensional test cases for both internal and external flow-field problems.

The external problems required the use of the CHIEF method in order to avoid possible instabilities as illustrated in the Paragraph 4.6 by using the least square technique. The N_{chief} points have been obtained by setting an additional number of 5% of the total number of points to be generated automatically and with a random procedure. Computations performed with and without the CHIEF method didn't show significant differences.

4.8.1. **Acoustic scattering by a 2D rigid cylinder**

Consider the acoustic scattering of a point monopole source by a rigid cylinder of radius *a*, with microphones located at the spherical coordinates *(r, θ)* and a source located at a distance r_q positioned on the axis at *θ=0* (Figure 4.2).

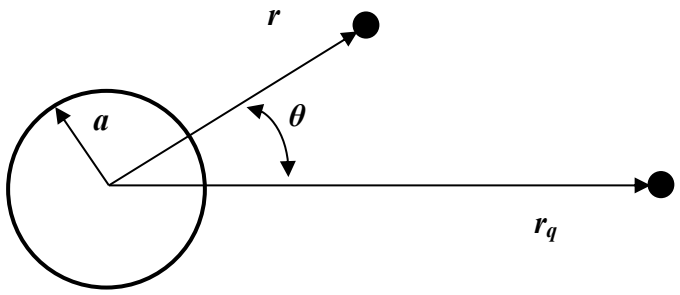

Figure 4.2 – Scheme of acoustic scattering of a point monopole source by a cylinder.

The analytical solution of the total pressure reads [21,22]:

$$\begin{cases} p(r,\theta|r_q,0) = \frac{i}{4}\sum_{m=-\infty}^{+\infty}\left[J(kr)H_m(kr_q) - \frac{J'_m(ka)}{H'_m(ka)}H_m(kr_q)H_m(kr)\right]e^{im\theta} & r \le r_q \\ p(r,\theta|r_q,0) = \frac{i}{4}\sum_{m=-\infty}^{+\infty}\left[J(kr_q)H_m(kr) - \frac{J'_m(ka)}{H'_m(ka)}H_m(kr_q)H_m(kr)\right]e^{im\theta} & r > r_q \end{cases}$$

where J_m and H_m are the Bessel and Henkel functions of the first kind and order m, whereas, J'_m and H'_m denote the derivative terms.

BEM analyses

With the aim of comparing BEM results to the analytical solution, a two dimensional cylinder with radius *a=1m* is considered.

A source point of unitary amplitude located at r_q*=2m* and a microphones arc of radius *r=1.5m* around the cylinder are used for comparison. The air properties are assumed to be *c* =340 *m/s* and ρ =1.225kg/m^3.

Concerning the BEM model, the cylinder is treated as rigid wall, $\frac{\partial p}{\partial n} = 0$, whereas the source point is modeled as a Dirac delta function applied at (r_q, *θ=0*). A mesh with 60 segment elements is considered (Figure 4.3).

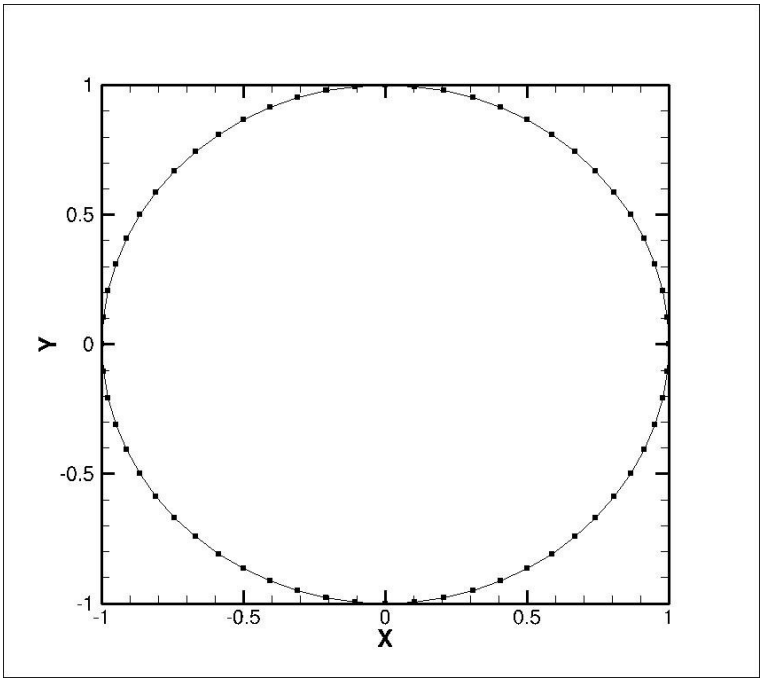

Figure 4.3 – Cylinder discretization with 60 segments.

BEM solutions are computed at three *ka* numbers, *1, 5* and *10*. With the aim of performing a mesh sensitivity study, three resolution levels of the mesh are considered. Thus, the coarse mesh is discretized with 60 segments, the medium mesh with 180 segments and the fine mesh with 360 segments.

Figure 4.4 illustrates the acoustic pressure in terms of real and imaginary part for the coarse mesh. Furthermore, the acoustic amplitude is compared for the three mesh levels underling the excellent agreement with the analytical solutions since with the medium mesh (Figure 4.5).

The BEM analysis, by using the coarse mesh, is computed also for a microphones grid in order to show the wave scattering contours plots of the real part of the acoustic pressure (Figure 4.6) for the three *ka* numbers.

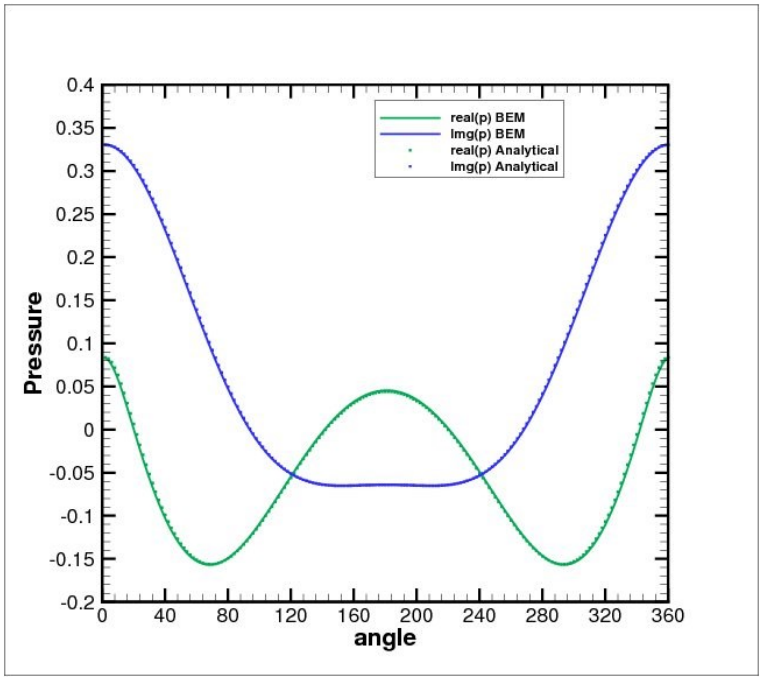

Figure 4.4a - Solution for ka=1

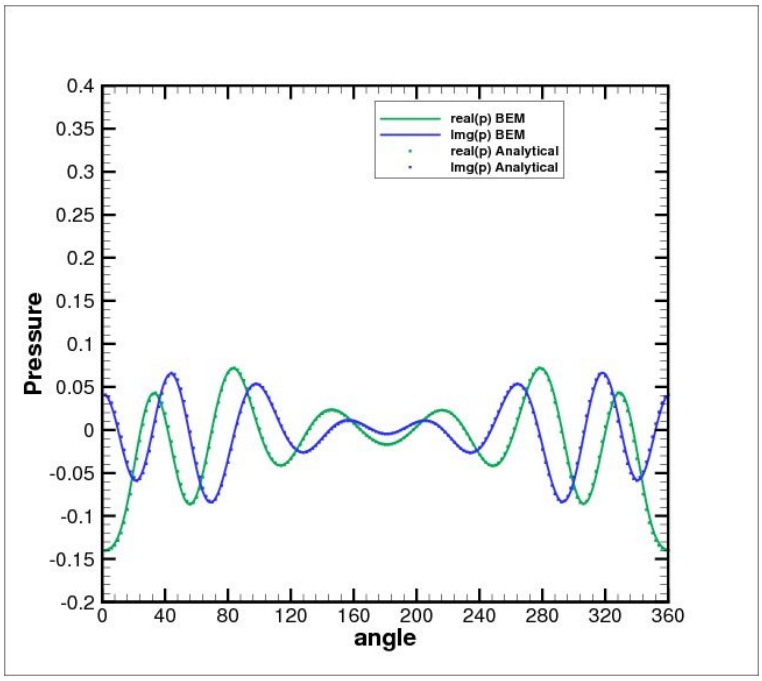

Figure 4.4b - Solution for ka=5

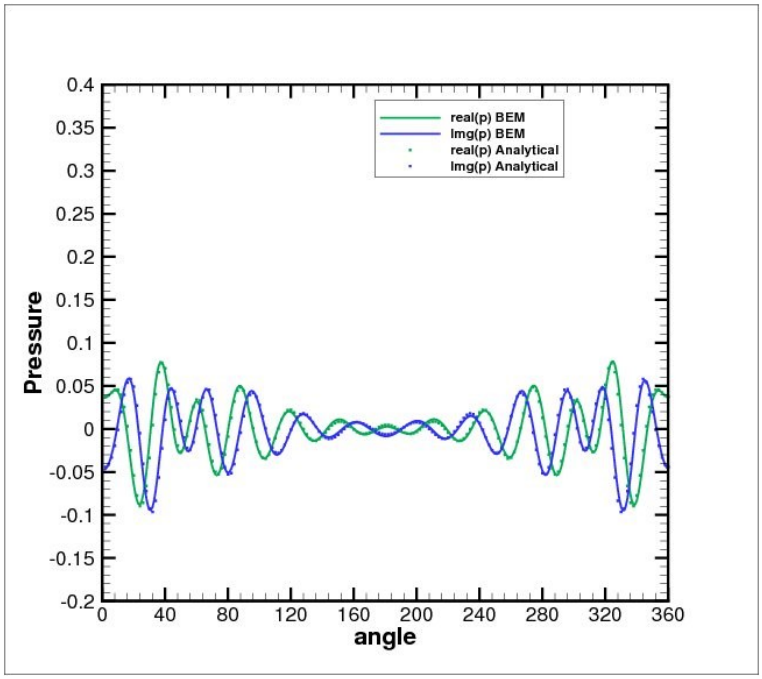

Figure 4.4c - Solution for ka=10

Figure 4.4 – Cylinder acoustic scattering - Real and Imaginary parts of the acoustic pressure. Comparison between analytical results (symbols) and numerical results with coarse mesh (continuous lines).

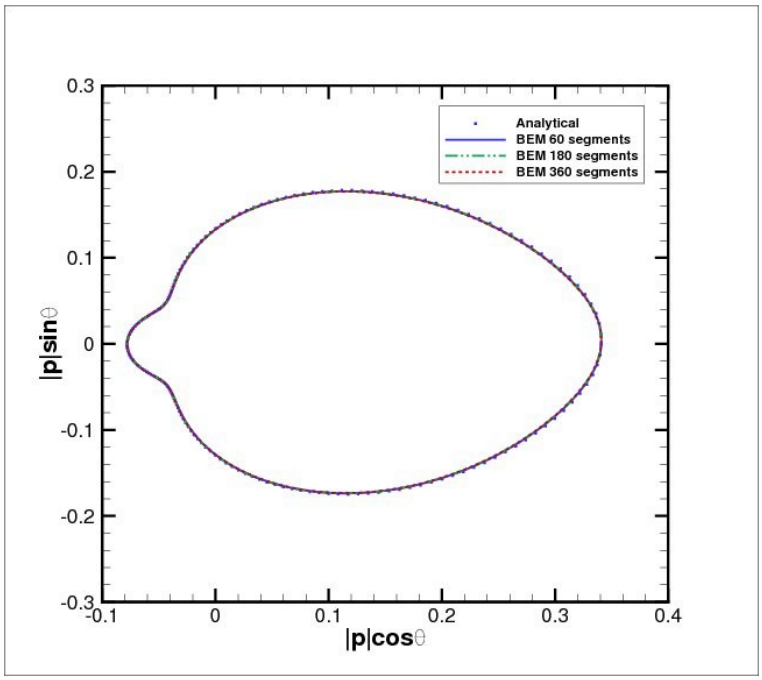

Figure 4.5a - Solution for ka=1

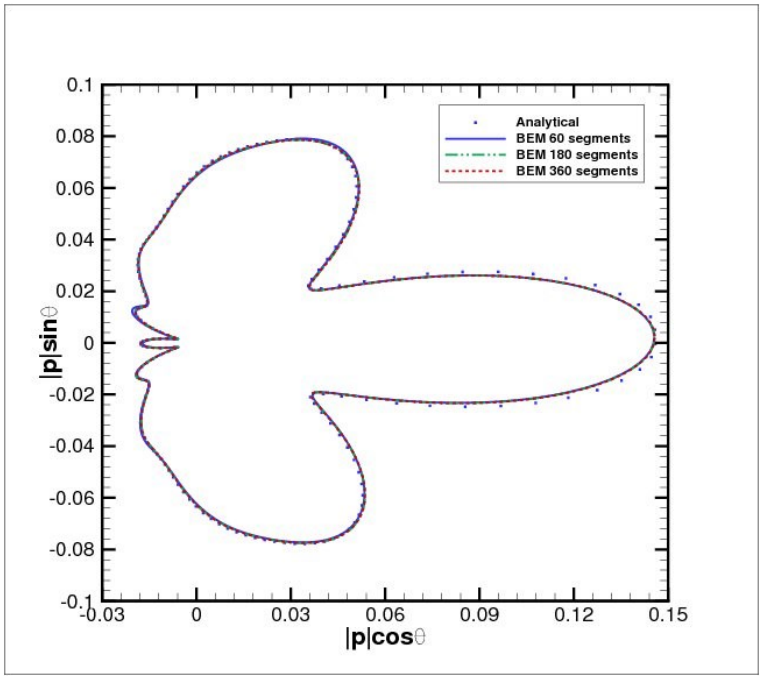

Figure 4.5b - Solution for ka=5

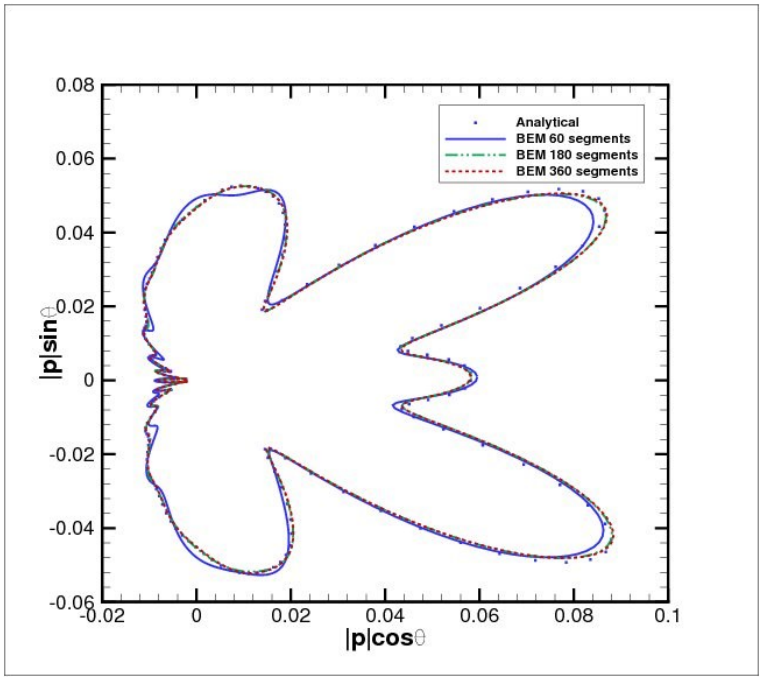

Figure 4.5c - Solution for ka=10

Figure 4.5 – Cylinder acoustic scattering – Pressure amplitude directivity. Comparison between analytical results (symbols), numerical results with coarse mesh (continuous lines), numerical results with medium mesh (dot-dashed lines) and numerical results with fine mesh (dashed lines).

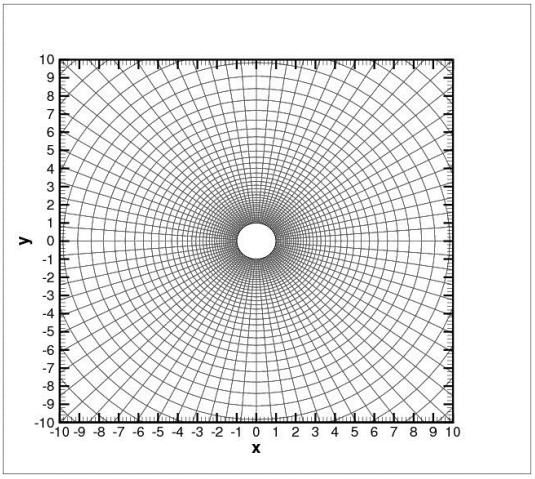

Figure 4.6a - Microphones grid

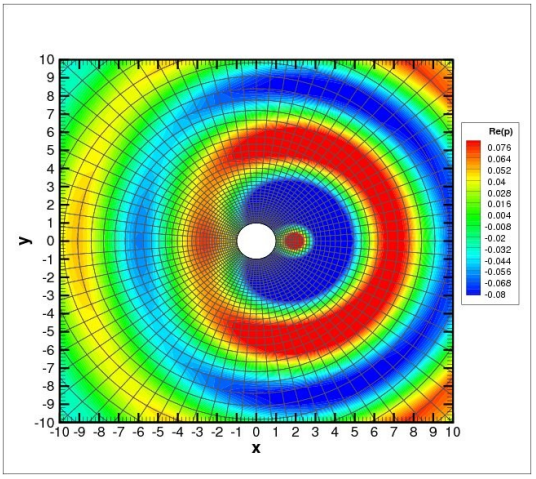

Figure 4.6b - Solution for ka=1

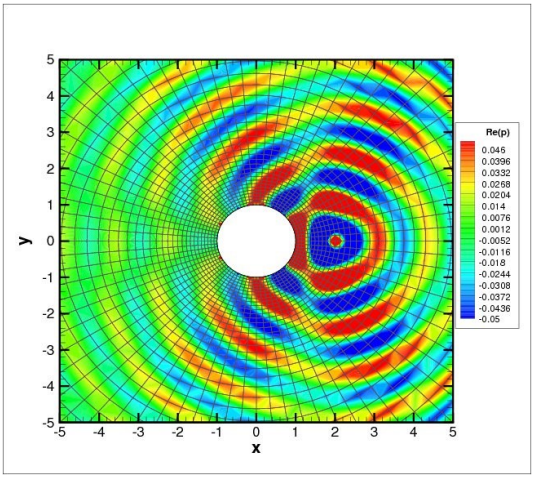

Figure 4.6c - Solution for ka=5

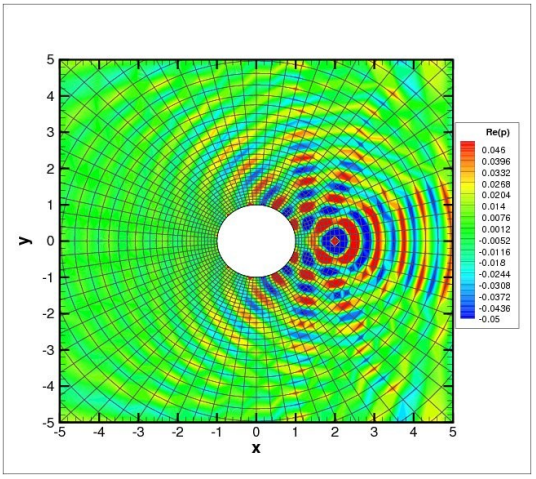

Figure 4.6d - Solution for ka=10

Figure 4.6 – Microphones grid and contour plots. Real part of the acoustic pressure at different ka numbers.

4.8.2. **Acoustic scattering by a 3D rigid sphere**

Consider the acoustic scattering of a point monopole source by a rigid sphere of radius *a*, with microphones located at the spherical coordinates *(r, θ)* and a source located at a distance r_q positioned on the axis at $\theta=0$ (Figure 4.7).

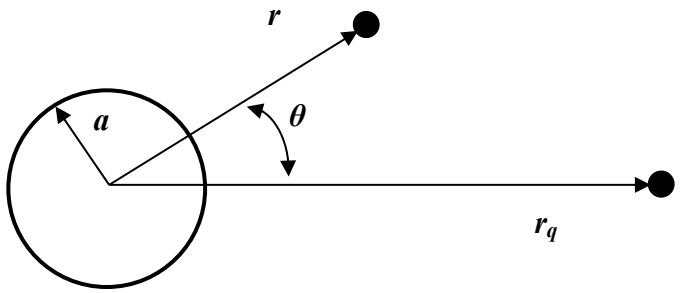

Figure 4.7 – Scheme of acoustic scattering of a point monopole source by a sphere.

The analytical solution of the total pressure reads [21,22]:

$$\begin{cases} p(r,\theta|r_q,0) = \dfrac{ik}{4\pi}\displaystyle\sum_{m=0}^{+\infty}(2m+1)\left[j_m(kr)h_m(kr_q) - \dfrac{j'_m(ka)}{h'_m(ka)}h_m(kr_q)h_m(kr)\right]P_m(\cos(\theta)) \quad r \le r_q \\ p(r,\theta|r_q,0) = \dfrac{ik}{4\pi}\displaystyle\sum_{m=0}^{+\infty}(2m+1)\left[j_m(kr_q)h(kr) - \dfrac{j'_m(ka)}{h'_m(ka)}h_m(kr_q)h_m(kr)\right]P_m(\cos(\theta)) \quad r > r_q \end{cases}$$

where j_m and h_m are the spherical Bessel and Henkel functions of the first kind and order m, whereas, j'_m and h'_m denote the derivative terms computed as:

$$j'_m(z) = -j_{m+1}(z) + \frac{m}{z}j_m(z)$$
$$h'_m(z) = -h_{m+1}(z) + \frac{m}{z}h_m(z)$$

The spherical Bessel and Henkel functions are related to the Bessel and Henkel functions by the following identities:

$$j_m(z) = \sqrt{\frac{\pi}{2z}}J_{m+\frac{1}{2}}(z) \quad , \quad h_m(z) = \sqrt{\frac{\pi}{2z}}H_{m+\frac{1}{2}}(z)$$

BEM analyses

With the aim of comparing BEM results to the analytical solution, a three dimensional sphere with radius *a=1m* is considered.

A source point of unitary amplitude located at r_q*=2m* and a microphones arc of radius *r=1.5m* around the sphere are used for comparison. The air properties are assumed to be *c* =340 *m/s* and ρ =1.225kg/m^3.

Concerning the BEM model, the sphere surface is treated as rigid wall, $\frac{\partial p}{\partial n} = 0$, whereas the source point is modeled as a Dirac delta function applied at ($r_{q,}$ θ*=0*). Two levels of discretization are considered resulting in a coarse mesh with 3480 quadrilateral elements and a refined mesh of about 19800 elements (Figure 4.8).

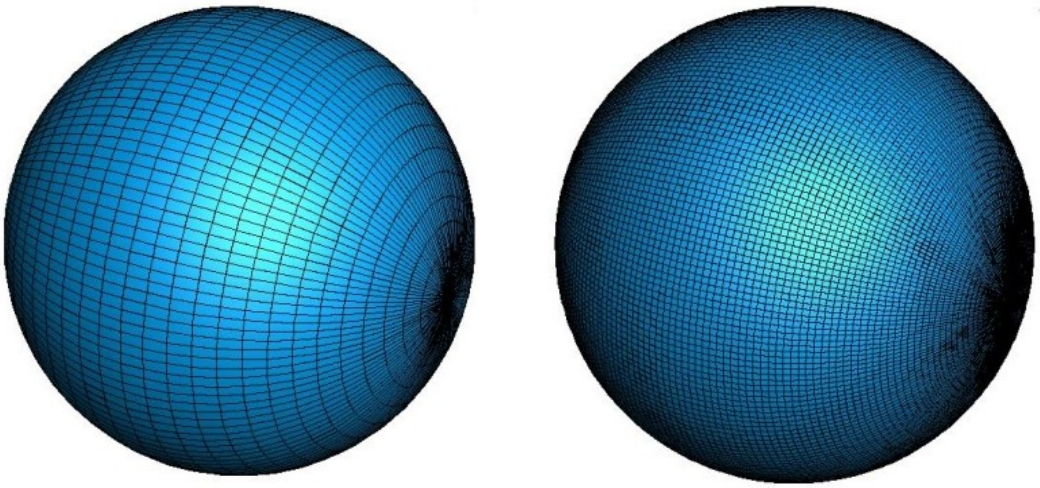

Figure 4.8a - Coarse grid *Figure 4.8b - Fine grid*

Figure 4.8 –Sphere grid.

Solutions are computed at three *ka* numbers, *1, 5* and *10,* comparing the acoustic pressure in terms of real and imaginary parts and in terms of acoustic amplitude. The mesh refinement study shows an excellent overlapping between the BEM and analytical solution even with the coarse mesh (Figure 4.9 and Figure 4.10).

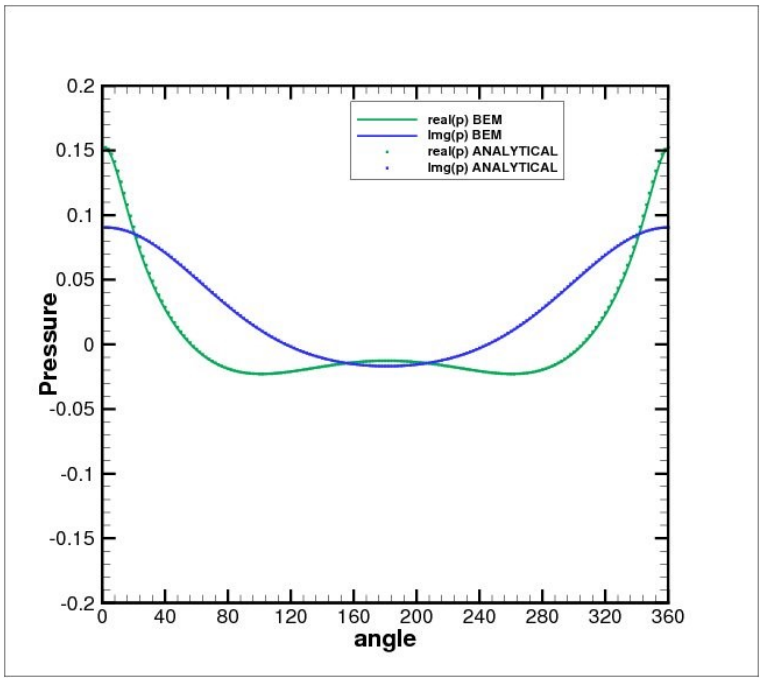

Figure 4.9a – Solution for ka=1

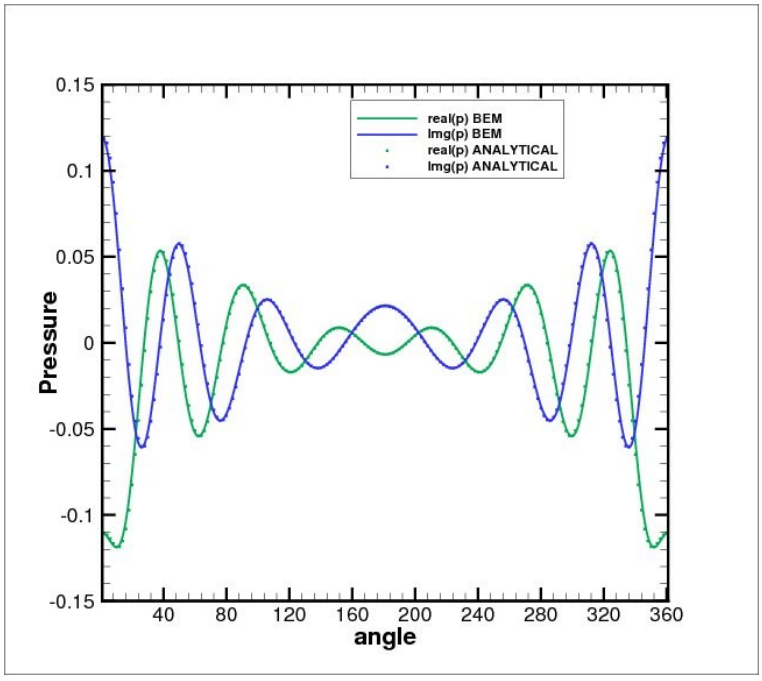

Figure 4.9b – Solution for $ka=5$

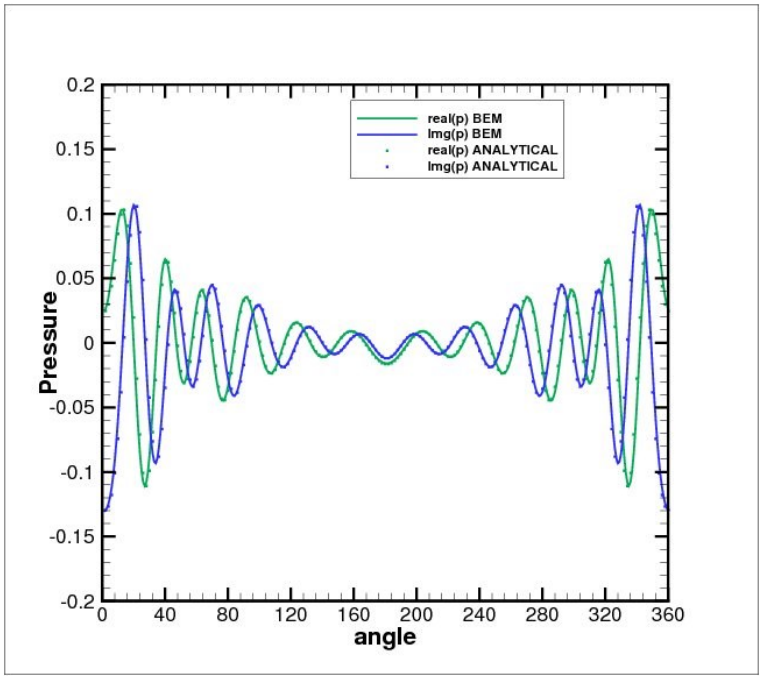

Figure 4.9c – Solution for $ka=10$

Figure 4.9 – Sphere acoustic scattering - Real and Imaginary parts of the acoustic pressure. Comparison between analytical results (symbols) and numerical results with coarse mesh (continuous lines).

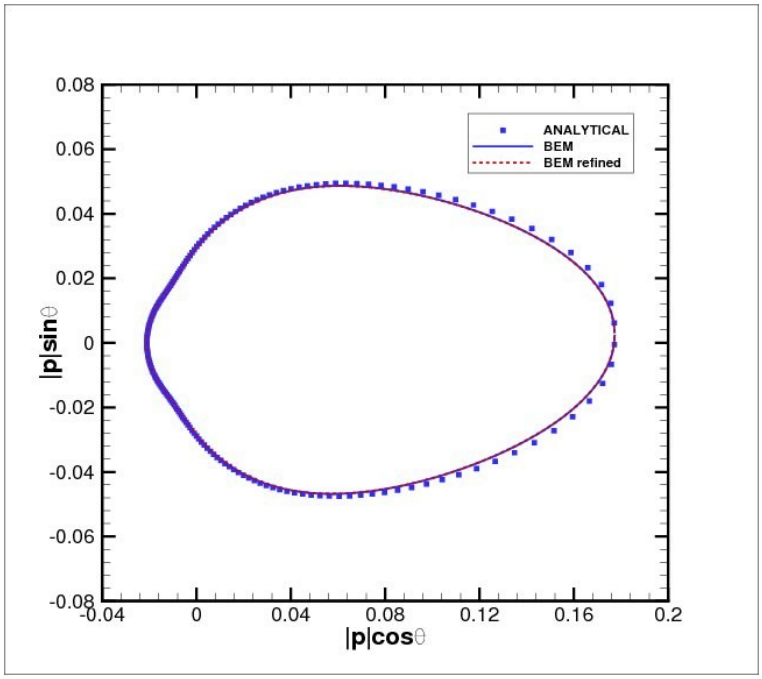

Figure 4.10a - Solution for ka=1

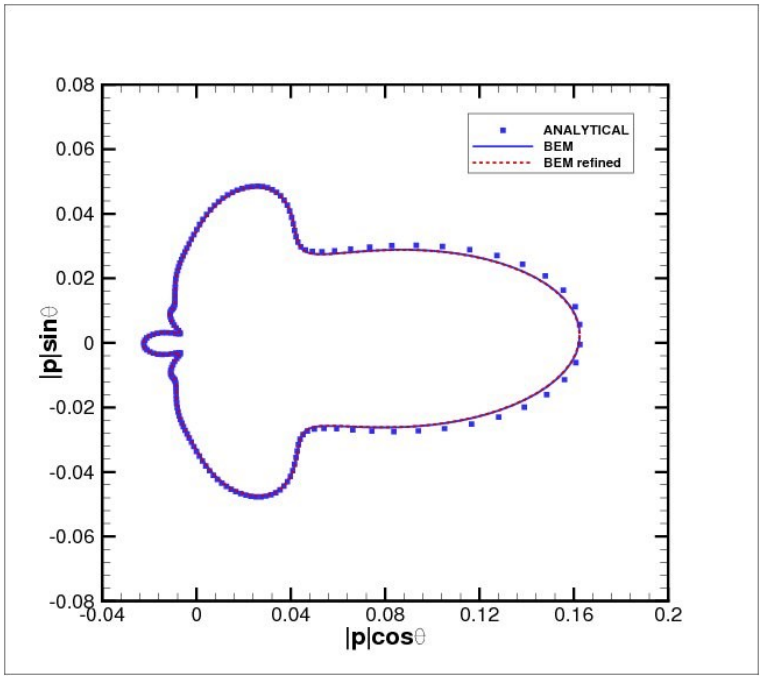

Figure 4.10b - Solution for ka=5

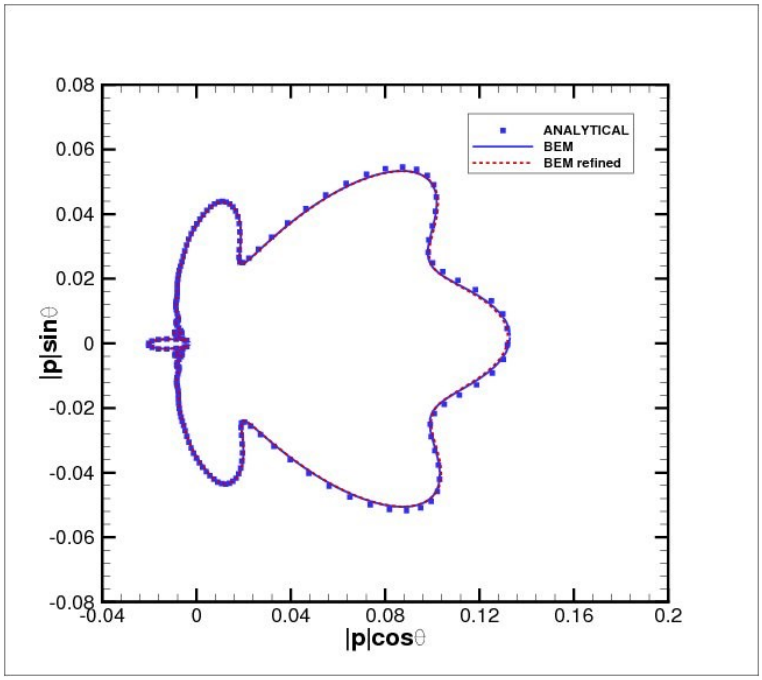

Figure 4.10c - Solution for ka=10

Figure 4.10 – Sphere acoustic scattering – Pressure amplitude directivity. Comparison between analytical results (symbols), numerical results with coarse mesh (continuous lines) and numerical results with fine mesh (dashed-lines).

4.8.3. **Acoustic duct**

Consider the wave transmission in a duct as shown in Figure 4.11.

The duct is driven by a uniform velocity, V_n, at $z=0$ and it is acoustically terminated by the surface acoustic impedance Z at the end $z=L$.

Figure 4.11 – Scheme of one dimensional duct.

The general solution of the one dimensional wave equation in z direction [23] assumes the form:

$$p = Ae^{ikz/(1+M_z)} + Be^{-ikz/(1-M_z)}$$

where A and B are the coefficients to be determined by means the boundary conditions, k is the acoustic wave number and M_z is the uniform flow Mach number.

Uniform velocity and Impedance boundary conditions

The first set of boundary conditions analyzed concerns the case of a vibrating wall at $z=0$ and a impedance boundary condition at $x=L$.

The set of boundary condition, using the $e^{-i\omega t}$ convention, reads:

$$\begin{cases} \dfrac{\partial p(z=0)}{\partial n} = i\rho\omega V_n \\ \dfrac{\partial p(z=L)}{\partial n} = -ik\,\dfrac{1}{\left[\dfrac{Z}{\rho c} - \bar{M}\bar{n}\right]}p + ik\,\dfrac{Z}{\left[\dfrac{Z}{\rho c} - \bar{M}\bar{n}\right]}V_{ns} \end{cases}$$

where V_n is the normal velocity applied at $z=0$, Z is the impedance and V_{ns} is the normal velocity applied at $z=L$.

Assuming the normal unit vector pointing inside the domain and V_{ns}=0, the boundary conditions, according to the z-axis, read:

$$\begin{cases} \dfrac{\partial p(x=0)}{\partial n} = i\rho\omega V_n \\ \dfrac{\partial p(x=L)}{\partial n} = -\dfrac{\partial p(x=L)}{\partial x} = ik\ \dfrac{1}{\left[\dfrac{Z}{\rho c} + M_z\right]} - ik\ \dfrac{Z}{\left[\dfrac{Z}{\rho c} + M_z\right]} V_{ns} \end{cases}$$

The *A* and *B* coefficients are obtained by substituting the general solution in the boundary conditions.

Uniform pressure and Impedance boundary conditions

The second set of boundary conditions analyzed concerns the case of a uniform pressure applied at *z=0* and an impedance boundary condition at *z=L* that reads:

$$\begin{cases} p(z=0) = p_0 \\ \dfrac{\partial p(z=L)}{\partial n} = -\dfrac{\partial p(z=L)}{\partial x} = ik\ \dfrac{1}{\left[\dfrac{Z}{\rho c} + M_z\right]} - ik\ \dfrac{Z}{\left[\dfrac{Z}{\rho c} + M_z\right]} V_{ns} \end{cases}$$

The *A* and *B* coefficients are obtained by substituting the general solution in the boundary conditions.

BEM analyses

With the aim of comparing numerical results to the analytical solution of the one dimensional wave equation, a three dimensional duct with square cross section is considered, with length *L=1m,* along the z-axis, and a section side *a=0.05m* (Figure 4.12).

For the BEM model the boundary conditions previously discussed are applied at *z=0* and *z=L* surface, whereas the lateral surfaces are treated as rigid wall, $\frac{\partial p}{\partial n} = 0$.

The air properties are assumed to be *c* =343 *m/s* and ρ =1.21kg/m^3.

Two BEM meshes at different refining levels are generated with respectively 2784 and 10354 triangular elements (Figure 4.12).

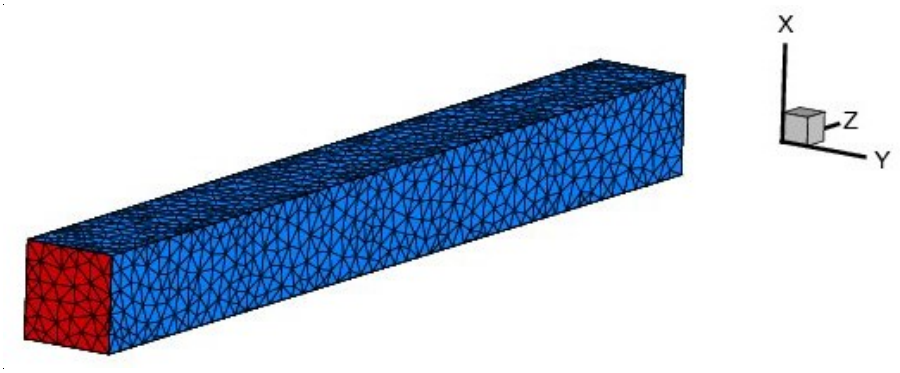

Figure 4.12a - Coarse grid

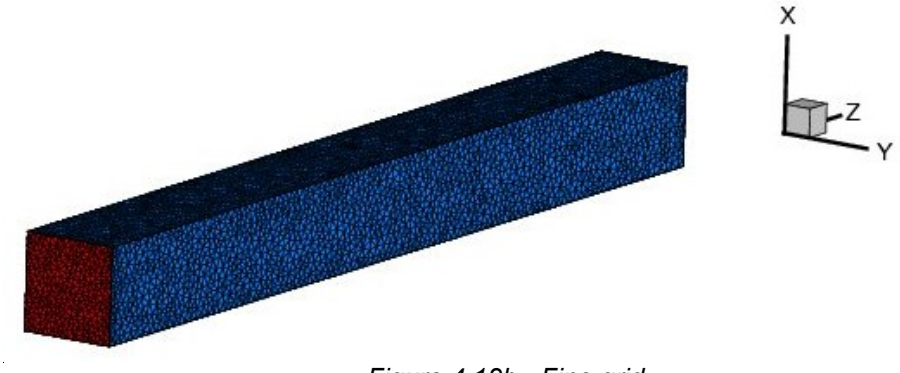

Figure 4.12b - Fine grid

Figure 4.12 –Square-section duct grid.

Solutions are computed at frequency $f = 2kHz$ and considering the terminal surface once as a rigid wall (impedance $Z=+\infty$) and once with the application of the characteristic impedance (impedance $Z=\rho c$). Solutions with zero mean flow ad a non zero uniform mean flow, $M=0.3$, are computed.

Figure 4.13a) shows the acoustic pressure amplitude along the z-axis with a uniform velocity, $V_n=1m/s$, at the inlet side and an infinite impedance at the outlet side, whereas, Figure 4.13b) highlights results achieved with characteristic impedance at the outlet side. The effect of the mesh refinement is also illustrated in Figure 4.13. The figures show an excellent agreement with the analytical solution and the curves are sufficiently overlapped except for $Z=\rho c$ condition for which the BEM solution exhibits moderate reflection effects. The characteristics impedance value produces a uniform pressure amplitude equal to $|p| = \rho c(1 + M_z)V_n$ as can be obtained by the analytical solution.

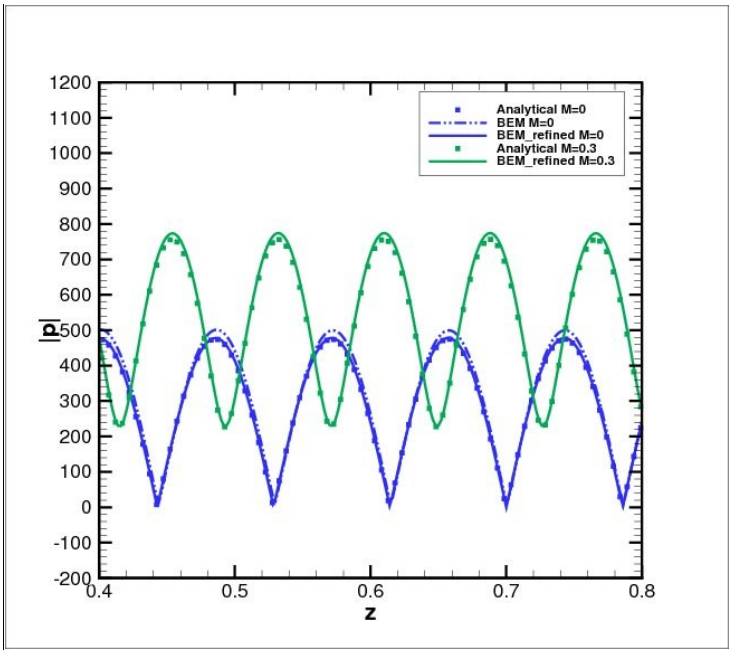

Figure 4.13a - Impedance $Z = +\infty$ at the outlet side.

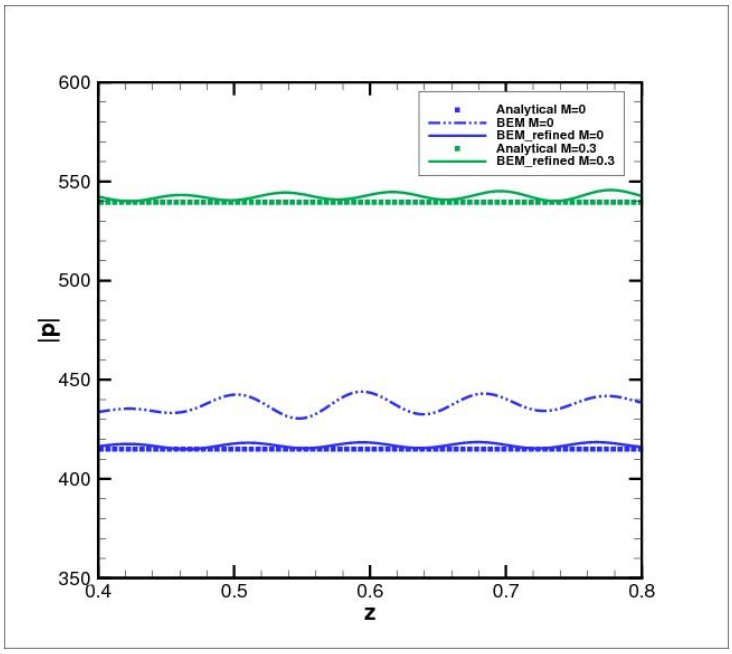

Figure 4.13b - Impedance $Z = \rho c$ at the outlet side.

Figure 4.13 – Duct acoustic solution. Vibrating boundary condition at the inlet side and impedance boundary condition at the outlet side. Comparison between analytical results (symbols), numerical results with coarse mesh (dot-dashed lines) and numerical results with fine mesh (continuous lines). Solutions at M=0 (blue lines) and M=0.3(green lines).

The same results and conclusions are achieved by applying a uniform pressure, p_0=*1Pa,* at the inlet surface, as shown in Figure 4.14. For this boundary condition, the characteristic impedance value produces a pressure amplitude equal to p_0.

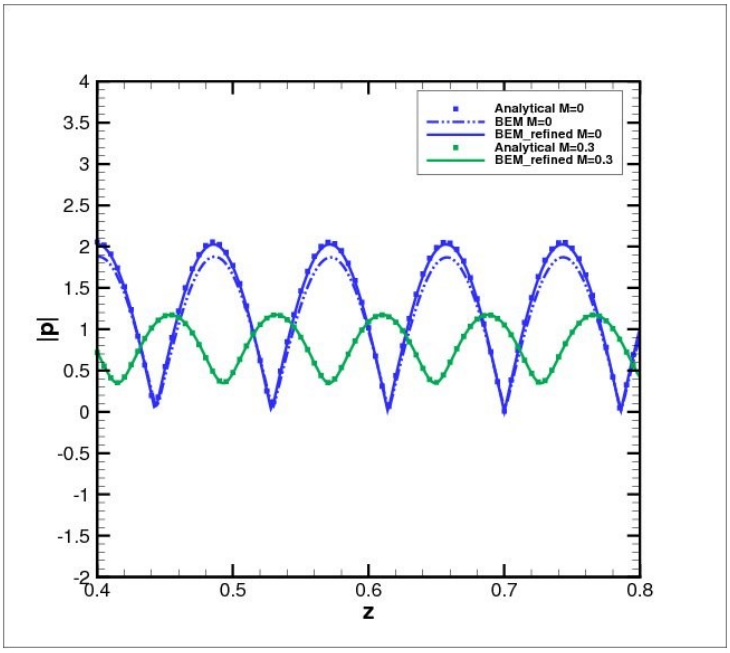

Figure 4.14a - Impedance $Z = +\infty$ at the outlet side.

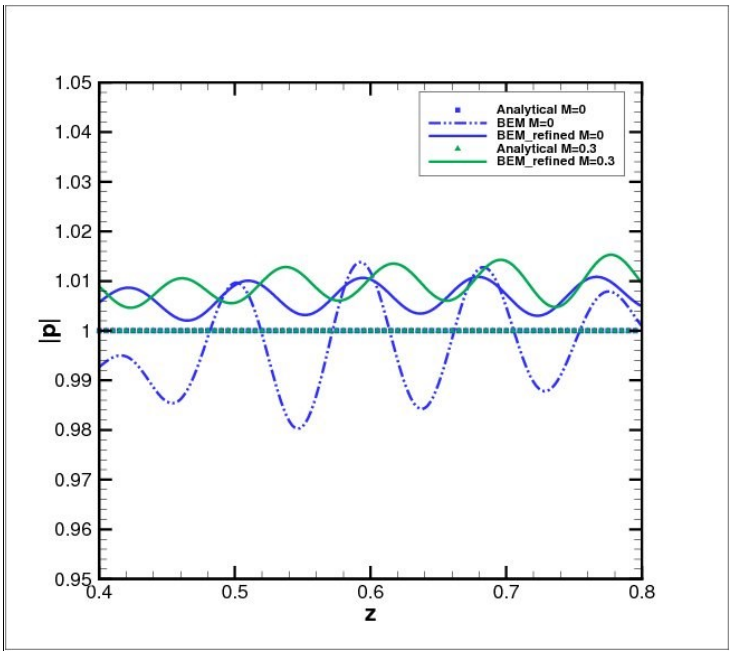

Figure 4.14b - Impedance $Z = \rho c$ at the outlet side.

Figure 4.14 – Duct acoustic solution. Dirichlet boundary condition at the inlet side and impedance boundary condition at the outlet side. Comparison between analytical results (symbols), numerical results with coarse mesh (dot-dashed lines) and numerical results with fine mesh (continuous lines). Solutions at M=0 (blue lines) and M=0.3(green lines).

4.8.4. **Naca0012 airfoil**

The trailing-edge scattering of a 2D airfoil is validated against the CIRA's FEM OptydB code [8,12,24].

With this aim, the same NACA0012 airfoil used in [25] is considered. The airfoil has a chord length of *0.*3048m and the air properties are assumed to be c =342.8m/s and ρ =1.244kg/m^3.Two different Mach numbers are investigated, *M=0* and *M=0.208.*

The effect of local velocity field near the airfoil is also evaluated with the FEM code by importing the local flow field from a RANS solution computed with the commercial CFD software Fluent by ANSYS at *M=0.208*. Figure 4.15 shows the local Mach variations in terms of $(M_\infty - M)/M_\infty$.

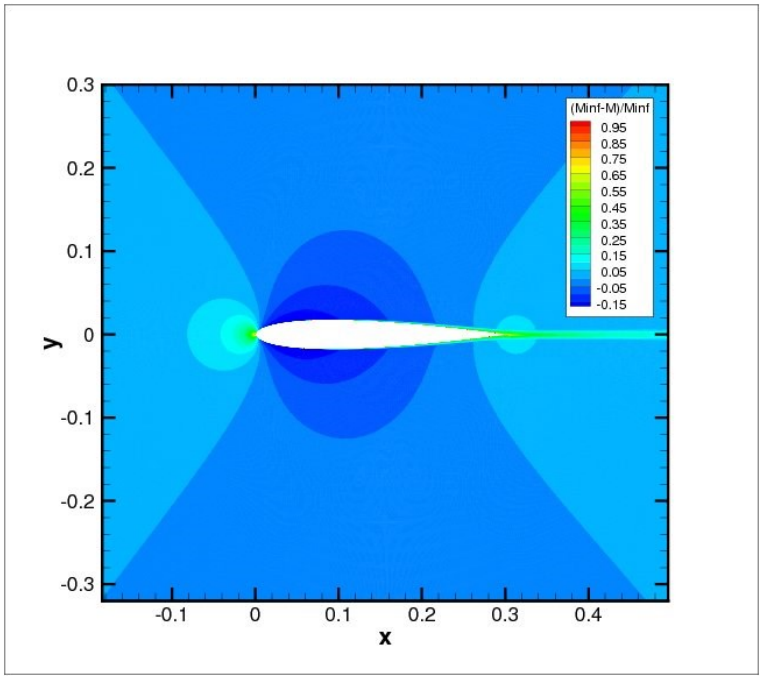

Figure 4.15 – Contour plot. NACA 0012 airfoil Mach number distribution.

The BEM mesh consists of 500 segment elements whereas the FEM one consists of 7444702 triangular elements. Figure 4.16 underlines the good agreement between the FEM and the BEM solutions also at mean flow condition. Furthermore, the comparison confirms that the effect of the not uniform mean flow predicted with the FEM code can be assumed negligible at relatively low Mach numbers.

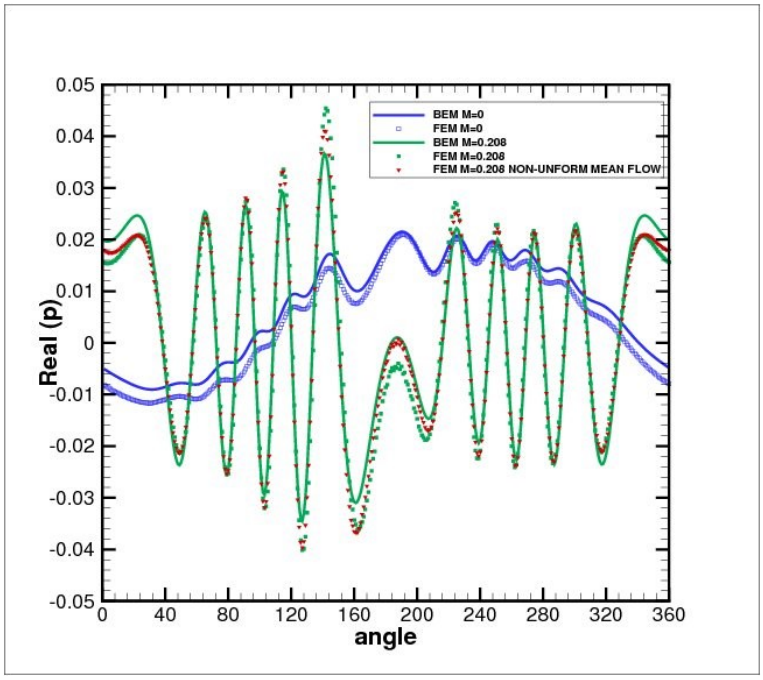

Figure 4.16a - Real part of the acoustic pressure

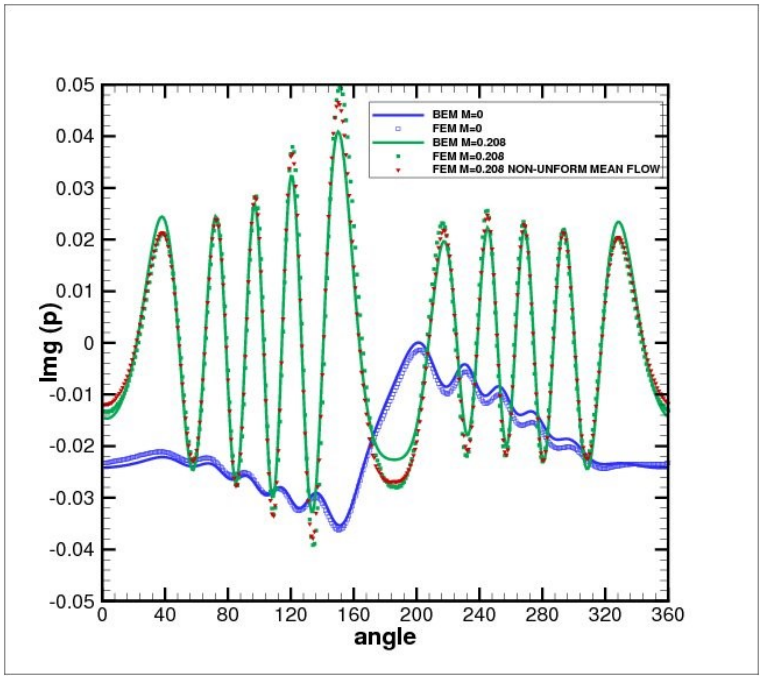

Figure 4.16b - Imaginary part of the acoustic pressure

Figure 4.16 –. Directivity patterns. Comparison between the FEM numerical results (symbols) and BEM numerical results (lines) at different Mach numbers. Solutions at M=0 (blue), M=0.208 (green) and M=0.208 with non-uniform mean flow (red).

5. Broadband noise source models

5.1. Introduction

While during departure the engine is recognized to be the main source of noise, the so-called airframe noise becomes more important during approach.
Airframe noise is the broadband noise radiated by the airplane due to the turbulent fluctuations occurring in proximity of the aircraft surfaces.

The two main sources for airframe noise are the landing gear and the high-lift devices. High-lift Devices (HLD) are deployed on the wing in order to increase the lift force, while the plane is decreasing in speed. These wing extensions often include a leading edge slat and one or multiple trailing edge flaps.

The sound generation mechanism from a Landing-Gear is due to the vortex-force generated by the quasi-periodic unsteady flow separation behind the different structural components. The resulting noise is of broadband nature, spanning over a wide interval in the audibility range.
Concerning the HLD broadband noise generation mechanism, it is due to the presence of a geometrical singularity. Indeed, the mechanism of conversion between turbulent kinetic energy and radiated acoustic energy is more effective than in the absence of solid surfaces (free-field turbulence noise) or in the absence of surface terminations (unbounded surface flow noise).
Moreover, the termination of a lifting surface is the place where an intense turbulent mixing occurs and where, as in the case of a flap side edge, the flow recirculation induces unsteady flow phenomena, i.e., shear-layer instabilities, vortex rollup, and interaction between the tip vortex and the side-edge corner [26]. Also Rotating devices employed for aircraft propulsion generate broadband noise due to the interaction between turbulence and blades.

The numerical simulation of these mechanisms through the solution of filtered Navier–Stokes equations, either using fully large-eddy simulation (LES) or hybrid

RANS–LES approaches such as the detached-eddy simulation (DES), is a major area of research [27,28,29,30,31,32,33]. However, because of the excessive computational cost, these types of simulations cannot be used for design purposes.

An alternative to LES or DES for wing HLD noise prediction consists of using RANS-based methods that can be used for multi-objective optimizations of wing profiles in conjunction with two-dimensional (2-D) steady Reynolds-averaged Navier–Stokes (RANS) computations and final three-dimensional (3-D) assessment of a wing low-noise design.
These allow to compute the far-field noise spectrum through an empirical source model and an analytical [34] or numerical [24,35,36,37] noise radiation model, or through the synthesis of stochastic flow fluctuations that are used to compute the right-hand side of an acoustic analogy equation [8,38,39].

Agarwall [35,36] presented a semi-empirical technique to estimate the broadband component of slat noise based on a modeling procedure similar to that used for jet noise predictions [40,41]. The noise in the far field is predicted by performing a convolution of numerical BEM Green's function with the modeled sources.

Furthermore, the stochastic approach for the prediction of broadband noise spectra from wall-bounded turbulent flows has received a great deal of interest in recent years, [38,39].
It was introduced by Kraichnan [42], and it is based on the idea that Fourier components of solenoidal velocity fluctuations can be sampled in the wave-number space from a prescribed mono-dimensional energy spectrum. An extension of the Fourier approach to simulate the different kinematics and statistics of large and small scale eddies was proposed by Fung et al. [43].
The revision and improvement of these methods for aeroacoustic applications have produced the stochastic noise generation and radiation (SNGR) method [44,45,46].
The SNGR method has been further revised by Casalino&Barbarino [8] where the control of the two-point correlation of the velocity fluctuations has been improved with respect to the standard SNGR model, based on the local value of the turbulence

correlation length, and by applying a digital filter to the stochastic variables of the model.

The advantages of the SNGR method are its simplicity and the possibility to control the spectral content of the velocity fluctuations.
A recognized drawback of the SNGR method is the computational time and memory occupation, due to the large amount of information to be produced and managed at each grid point.

In all RANS-based methods, the RANS turbulent kinetic energy and dissipation rate are used to define the magnitude and the length/time scales of the noise sources. The main limitation of any RANS-based method is that it follows from several modeling assumptions in the derivation of the source term or in the synthesis of the stochastic flow fluctuations, and this restricts the universal character of the method. As a consequence, RANS-based methods require the calibration of some model parameters through specific experimental campaigns.

Among different HLD broadband noise generation mechanisms, one of the main source of airframe noise is represented by the wing trailing-edge noise due to the interaction between the turbulence in the boundary layer and the trailing edge (TE), usually referred as *self-noise*.
The mechanism of TE noise generation and radiation has been extensively investigated in the past.
A hybrid analytical-empirical method in frequency domain was developed for the first time in 1975 by Amiet for an airfoil [47,48]. This method consists in relating the noise spectrum to the wall pressure spectrum through an airfoil scattering function. In order to use a wall pressure distribution with the same characteristics it would have in the absence of the TE, Amiet assumed that the turbulence is statistically stationary when convected past the TE.
In recent years TE broadband noise models based on Amiet formulation have been developed and validated against experimental data by Roger & Moreau [49,50] and by Blandeau & Joseph [51,52] in practical cases that are representative of aircraft wings, wind turbines, helicopter blades and cooling fan systems.

The original idea applied to an airfoil was also extended and successfully applied to rotor broadband noise prediction [53]. The extension of Amiet airfoil self-noise model to a rotating blade is made through a strip approach in which spanwise blade segments are treated as uncorrelated two-dimensional source.
Döppler effects are accounted for by considering the blade segment rotational velocity. The same formulation has been used by Pagano et al. [54] to compute the broadband noise generated by a propeller in a pusher aircraft configuration.

Casalino&Barbarino [24], for a 2D High-Lift Wing design, instead of using the RANS solution in the field to compute the source term of a wave equation introduced an alternative approach to compute the self-noise of a NACA-0012 airfoil. They used the boundary-layer properties in proximity of the trailing edge from a RANS solution to estimate the wall-pressure spectrum through a semi-empirical model [53,55,56,57,58]. This approach was used to compute an equivalent pressure to be finally applied as boundary condition of a wave equation solved with a FEM technique.

More recently, Casper and Farassat [59,60,61,62] used the analytical scattering equation and the semi-empirical turbulence spectra to synthesize a stochastic pressure distribution in time domain. The dipoles distribution induced by turbulence was then propagated by means of the numerical integration of the FW-H equation in the time domain and applied to the airfoil noise prediction. This hybrid analytical/numerical approach was applied for the first time by Barbarino&Casalino [63] to a propeller, and the results were verified against the analytical results obtained in the frequency domain by means of a strip approach.

This Chapter deals with a few part of the source models described in literature.
Paragraph 5.2 deals with the introduction to the self-noise prediction based on the Amiet analytical model [47,48] and the extension of the analytical model to the BEM or FEM numerical scattering [24].

Paragraphs 5.3 and 5.4 propose more general approaches for broadband noise prediction by using the RANS-based models: respectively the SNGR [8] and the Agarwal [35,36] approaches.

Finally, Paragraph 5.5 shows the application of the abovementioned methods to the trailing-edge noise prediction of a NACA0012 airfoil.

5.2. Semi-analytical and Hybrid Empirical/Numerical models for self-noise prediction

Trailing edge noise (or self-noise) is due to the scattering of boundary layer vortical disturbances at the geometrical discontinuity of the trailing edge.

The pressure fluctuations, in the boundary layer, generate lift fluctuations on the airfoil. According to the acoustic analogy these fluctuations can be seen as elementary dipoles that generates noise (Figure 5.1).

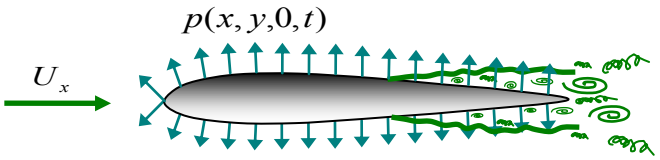

Figure 5.1 – Trailing edge noise mechanism.

Following Amiet and co-workers [47,48,53]. and Roger & Moreau [49,50] the TE noise power spectral density (PSD) at the observer x and the frequency ω, of the pressure fluctuation on the surface of a finite chord flat plate induced by the wave generated at the trailing edge reads:

$$S_{pp}^{TE}(\bar{x},\omega)=\left(\frac{kLz}{4\pi\sigma^2}\right)^2\frac{c}{2U_c}\int_{-\infty}^{\infty}\Phi_{pp}\left(\frac{\omega}{U_c},\overline{K}_y\right)\frac{\sin^2\left[\frac{L}{c}\left(\overline{K}_y-\bar{k}\frac{y}{\sigma}\right)\right]}{\left(\frac{L}{c}\right)^2\left(\overline{K}_y-\bar{k}\frac{y}{\sigma}\right)^2}\left|I_{TE}\left(\frac{\omega}{U_c},\overline{K}_y\right)\right|^2 d\overline{K}_y \qquad \textbf{(5.1)}$$

where $\bar{K}_x = K_x c/2$ and $\bar{K}_y = K_y c/2$ are the dimensionless gust wavenumbers, $\bar{k} = \omega c/(2c_0)$ is the non-dimensional acoustic wavenumber, $\sigma = \sqrt{x^2 + \beta(y^2 + z^2)}$ is the Prandtl-Glauert transformed distance from the TE, $\beta = \sqrt{1 - {M_x}^2}$ and I_{TE} is the radiation integral function.

This consists of a main contribution I_{1TE} derived from the assumption of a semi-infinite flat plate (high frequency approximation), and a term I_{2TE} accounting for the wave back reflection at the LE (finite chord length correction). These two contributions read:

$$I_{TE1} = -\frac{e^{2iC}}{iC}\left\{(1+i)e^{-2iC}\sqrt{\frac{B}{B-C}}E^*[2(B-C)] - (1+i)E^*[2B] + 1\right\} \tag{5.2}$$

$$\frac{1}{H}I_{TE2} = \left\{e^{4i\bar{\kappa}}\left[1-(1+i)E^*(4\bar{\kappa})\right]\right\}^c - e^{2iD} + i[D + \bar{K}_x + M_x\bar{\mu} - \bar{\kappa}]G \tag{5.3}$$

where the quantities are defined as follows:

$$C = \bar{K}_x - \bar{\mu}\left(\frac{x}{\sigma} - M_x\right)$$

$$B = \bar{K}_x - \bar{\mu}M_x + \bar{\kappa}$$

$$H = \frac{(1+i)e^{-4i\bar{\kappa}}(1-{\Theta_1}^2)}{2\sqrt{\pi}(\alpha-1)\bar{K}_x\sqrt{B}}$$

$$D = \bar{\kappa} - \bar{\mu}\frac{x}{\sigma}$$

$$G = (1+\varepsilon)e^{i(2\bar{\kappa}+D)}\frac{\sin(D-2\bar{\kappa})}{D-2\bar{\kappa}} + (1-\varepsilon)e^{i(-2\bar{\kappa}+D)}\frac{\sin(D+2\bar{\kappa})}{D+2\bar{\kappa}}$$
$$+\frac{(1+\varepsilon)(1-i)}{2(D-2\bar{\kappa})}e^{4i\bar{\kappa}}E^*(4\bar{\kappa}) - \frac{(1-\varepsilon)(1+i)}{2(D+2\bar{\kappa})}e^{4i\bar{\kappa}}E(4\bar{\kappa})$$
$$+\frac{e^{2iD}}{2}\sqrt{\frac{2\bar{\kappa}}{D}}E^*(2D)\left[\frac{(1-\varepsilon)(1+i)}{D+2\bar{\kappa}} - \frac{(1+\varepsilon)(1-i)}{D-2\bar{\kappa}}\right]$$

$$\alpha = \frac{U_x}{U_c}$$

$$\varepsilon = \left(1 + 1/(4\bar{\kappa})\right)^{-1/2}$$

$$\bar{\kappa}^2 = \bar{\mu}^2 - \bar{K}_y{}^2 / \beta^2$$

$$\bar{\mu} = \bar{K}_x M_x / \beta^2$$

The notation $\{\ \}^c$ means that the imaginary part must be multiplied by the factor ε. Figure 5.2 shows an airfoil section of chord c and span length L and the reference system used in the equation.

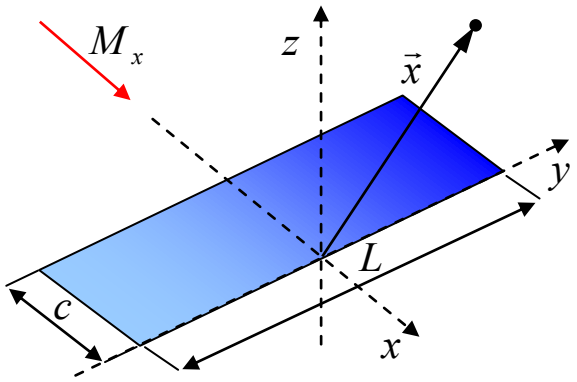

Figure 5.2 – Coordinates system of the trailing-edge noise model.

The wave-number frequency spectrum Φ_{pp} can be related to the frequency spectrum ϕ_{pp} and to the spanwise correlation length l_y by writing:

$$\Phi_{pp}\left(\frac{\omega}{U_c}, K_y\right) = \frac{U_c}{\pi}\phi_{pp}(\omega) l_y(\omega, K_y) \qquad \textbf{(5.4)}$$

where the spanwise correlation length can be estimated using the Corcos' formula that reads:

$$l_y(\omega, K_y) = \frac{\omega/(bU_c)}{K_y{}^2 + \omega^2/(bU_c)^2} \qquad \textbf{(5.5)}$$

with b denoting an empirical spanwise correlation constant.

It can be demonstrated that in the hypothesis of infinite span, only one spanwise wave number contributes to the wall-pressure fluctuations, $\overline{K}_y = \bar{k}(y/\sigma)$, and this is proportional to the distance from the midspan plane. In fact, in the hypothesis of infinite span-wise length *L*, the cardinal sine can be substituted by the Dirac distribution by means of:

$$\frac{\sin^2\left[\frac{L}{c}\left(\overline{K}_y - \bar{k}\frac{y}{\sigma}\right)\right]}{\left(\frac{L}{c}\right)^2\left(\overline{K}_y - \bar{k}\frac{y}{\sigma}\right)^2} \approx \pi\frac{c}{L}\delta\left[\left(\overline{K}_y - \bar{k}\frac{y}{\sigma}\right)\right]$$

Considering the Dirac distribution property that:

$$\int_{-\infty}^{\infty}\Phi_{pp}\left(\frac{\omega}{U_c},\overline{K}_y\right)\delta\left[\left(\overline{K}_y - \bar{k}\frac{y}{\sigma}\right)\right]\left|I_{TE}\left(\frac{\omega}{U_c},\overline{K}_y\right)\right|^2 d\overline{K}_y = \Phi_{pp}\left(\frac{\omega}{U_c},\bar{k}\frac{y}{\sigma}\right)\left|I_{TE}\left(\frac{\omega}{U_c},\bar{k}\frac{y}{\sigma}\right)\right|^2$$

The large aspect-ratio approximation can be written as:

$$S_{pp}{}^{TE}(\bar{x},\omega) = \left(\frac{kcz}{4\pi\sigma^2}\right)^2\frac{L}{2}\frac{\pi}{U_c}\Phi_{pp}\left(\frac{\omega}{U_c},\bar{k}\frac{y}{\sigma}\right)\left|I_{TE}\left(\frac{\omega}{U_c},\bar{k}\frac{y}{\sigma}\right)\right|^2 \qquad \textbf{(5.6)}$$

The above equation shows that for a microphone symmetrically placed respect to the airfoil (y=0) just the wavenumber $K_y = 0$ contributes to the noise propagation.

Considering the equation of the wave-number spectrum as function of the frequency wall pressure spectrum, $\phi_{pp}(\omega)$, the PSD becomes:

$$S_{pp}{}^{TE}(\bar{x},\omega) = \left(\frac{kcz}{4\pi\sigma^2}\right)^2\frac{L}{2}\phi_{pp}(\omega)l_y\left(\omega,\bar{k}\frac{y}{\sigma}\right)\left|I_{TE}\left(\frac{\omega}{U_c},\bar{k}\frac{y}{\sigma}\right)\right|^2 \qquad \textbf{(5.7)}$$

To extend the results of the airfoil analytical model to a generic blade, a strip theory approach is applied. The blade is divided into elements (Figure 5.3) which are

characterized by different values in spanwise direction of relative mean flow, local incidence angle, geometrical shape and statistical parameters of the fluctuations. The overall far field sound is calculated by summing each blade element noise contribution and by assuming uncorrelated sources [54].

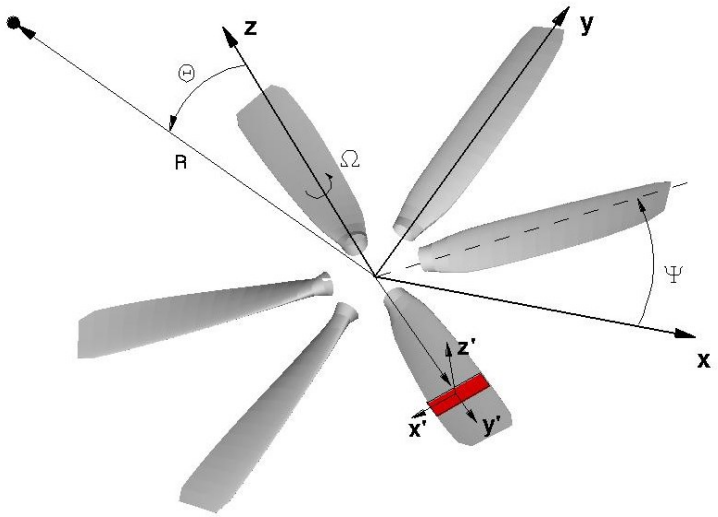

Figure 5.3 – Rotor extension using a blade element theory.

Furthermore, a frequency-shift correction is applied to each section in order to account for the Döppler effects by writing:

$$\frac{\omega_e(\psi)}{\omega} = 1 + \frac{M_t \sin\Theta \sin\psi}{\sqrt{1 - M_z{}^2 \sin^2\Theta}} \tag{5.8}$$

where M_z is the axial Mach number and M_t is the local spanwise tangential Mach number and Ψ denotes the azimuthal blade location.

Finally, the overall noise is computed by assuming fully uncorrelated strip sources and averaging over all the angular positions of the B propeller blades, i.e.:

$$S_{pp}(\bar{x}, \omega) = \frac{B}{2\pi} \int_0^{2\pi} \frac{\omega_e(\psi)}{\omega} S_{pp}{}^{\psi}(\bar{x}, \omega_e) d\psi \tag{5.9}$$

The wall-pressure PSD can be estimated through specific measurements. Experimental determinations of the frequency wall pressure spectrum caused by turbulent fluctuations and made by a lot of authors showed a relation with the boundary layer quantities of the inner and outer regions. Indeed, normalizing the wall pressure spectrum with the inner or outer boundary layer variables, the experimental points showed collapsing to a curve with a characteristic law.

Since the low frequency part of the pressure spectrum is affected by the outer region of the boundary layer (boundary layer displacement thickness and boundary layer asymptotic velocity) and the high frequency part is affected by the inner region (wall shear stress and fluid viscosity) an effective normalization making use of mixed variables is expected.

These considerations have been used in the past by a lot of authors to develop models for the frequency spectrum of wall pressure fluctuations beneath a turbulent boundary layer as a function of the boundary layer quantities. Different models have been developed normalizing the spectrum with the inner variables [53] the mixed variables [55] and taking into account the Reynolds number effect [56].

More recently, the adverse pressure gradient effect on the statistical properties of the wall pressure has been recognized [57].

Schlinker and Amiet [53] proposed an analytical formulation by using the outer boundary-layer scaling quantities and fitting the surface pressure spectrum data of Willmarth and Roos [58]:

$$\frac{\phi_{pp}\left(\frac{\omega\delta^*}{U_e}\right)}{(\frac{1}{2}\rho_0 U_e{}^2)^2\frac{\delta^*}{U_e}} = \frac{2\cdot 10^{-5}}{1+\left(\frac{\omega\delta^*}{U_e}\right)+0.217\left(\frac{\omega\delta^*}{U_e}\right)^2+0.00562\left(\frac{\omega\delta^*}{U_e}\right)^4} \qquad \textbf{(5.10)}$$

where δ^* and U_e are respectively boundary layer displacement thickness and boundary layer asymptotic velocity.

To reproduce the wall-pressure spectrum at the TE of a NACA0012 airfoil, since the above model is for a zero pressure gradient flat plate, Schlinker and Amiet proposed

an empirical correction function for a realistic airfoil that multiplies the flat plate wall pressure spectrum.

Rozenberg [57] proposed an improved wall pressure spectrum model, based on Goody's model [56], to take into account also the pressure gradient effect that can increase the wall pressure spectrum up to about 10dB. The model considers the normalization by means the mixed boundary layer variables and takes also into account the Reynolds number effect.

An alternative hybrid approach, illustrated by Casalino & Barbarino in [24], consists in the use of the wall-pressure PSD in proximity of the trailing edge in order to define a value for the acoustic pressure to be used as Dirichlet Boundary condition of a wave equation (see Paragraph 4.4.1).

In the frequency band $[f_1, f_2]$, the wall-pressure root mean square can be related to the Wall Pressure Spectrum of a semi-empirical model (see equation (5.10)) by:

$$p_{rms} = \sqrt{\int_{f_1}^{f_2} \phi_{pp}(2\pi f) df} \tag{5.11}$$

Since the Dirichlet boundary condition is imposed only in a few surface cells very close to the trailing edges, the wall pressure root mean square can be assimilated to the magnitude of a Fourier component p_0 with phase arbitrarily set to zero (see Paragraph 4.4.1).

5.3. SNGR approach

Following the concept proposed by Kraichnan [42], turbulent velocity fluctuation can be computed as a sum of Fourier components; that is,

$$\boldsymbol{u}'(\boldsymbol{x}, t) = 2 \sum_{n=1}^{N_F} \hat{u}_n cos\{\boldsymbol{k_n} \cdot (\boldsymbol{x} - \varrho \boldsymbol{U} t) + \psi_n\} \boldsymbol{\sigma_n} \tag{5.12}$$

where $\hat{\boldsymbol{u}}_{\boldsymbol{n}}$ ψ_n $\boldsymbol{\sigma_n}$ are the magnitude, phase, and direction of the nth Fourier component, respectively. As proposed by Bailly and Juvé [45], each Fourier mode is

supposed to be convected at the local mean-flow velocity $\boldsymbol{U}$, corrected by the vortex convection velocity ratio ϱ. This factor may account for the wall induction effect that reduces the vortex convection velocity with respect to the mean-flow velocity at the location of the vortex core. For the self-noise prediction, the value $\varrho = 0.9$ is assumed. The factor may also account for the vortical induction in a jet shear layer, but this effect is negligible for low-speed subsonic jets. Notice that the scalar product $\varrho \boldsymbol{k_n} \cdot \boldsymbol{U}$ accounts for the local time variation of the velocity field. Assuming incompressibility, the zero divergence condition applied to Eq. (5.12) results in the relationship $\boldsymbol{k_n} \cdot \boldsymbol{\sigma_n} = \boldsymbol{0}$, stating that the wave vector is perpendicular to the velocity vector.

By supposing that the turbulent flow field is isotropic, the magnitude of the n-th Fourier mode is related to the mono-dimensional energy spectrum *E(k)* by the expression, $\hat{u}_n = \sqrt{E(k_n)\Delta k_n}$ where k_n and Δk_n are the wave number and the corresponding band of the n-th mode. The Von Kármán–Pao isotropic turbulence spectrum is assumed; that is:

$$E(k) = A(2/3)(K/k_e)(k/k_e)^4 exp\left[-2(k/k_\eta)\right][1 + (k/k_e)^2]^{-17/6} \qquad \textbf{(5.13)}$$

where *K* is the turbulent kinetic energy, *A* is a numerical constant, k_e is the wave number of maximum energy, and $k_\eta = \epsilon^{1/4}\upsilon^{-3/4}$ is the Kolmogorov wave number. The constants *A* and $k_e$can be determined by equating the integral energy and the integral length scale derived from Eq. (5.13) to the RANS quantities *K* and $L_T = c_1 u'^3/\epsilon$, respectively, $u' = \sqrt{2K/3}$ being the isotropic turbulent velocity and c_1 a tuning parameter of the method.

This provides $A \cong 1.453$ and$k_e = 0.747/L_T$. The parameter $c_1$allows to tune the RANS turbulent integral length scale of the large-scale eddies. Its value is, by definition, close to 1, but its optimal value depends on the turbulent flow structure and conditions and on the RANS turbulence model.

The stochastic velocity perturbation field can be generated by choosing probability density functions for all the random variables involved in Eq. (5.12).

These stochastic variables are the angles φ_n and $\theta_n$defining the direction of the wave vector $\boldsymbol{k_n}$, as sketched in Fig. (5.12); the angle $\alpha_n$defining the direction of the unit

vector $\boldsymbol{\sigma_n}$in a plane orthogonal to $\boldsymbol{k_n}$; and finally the phase angle ψ_n. By requiring that the wave vector is uniformly distributed in the 3-D wave-number space provides the following probability densities:

$$\wp(\varphi_n) = \frac{1}{2\pi} \quad with \quad -\pi \leq \varphi_n \leq \pi \tag{5.14}$$

$$\wp(\theta_n) = \cos(\theta_n)/2 \quad with \quad -\pi/2 \leq \theta_n \leq \pi/2 \tag{5.15}$$

Analogously, by supposing that the $\boldsymbol{\sigma_n}$ vector is uniformly distributed in the plane normal to $\boldsymbol{k_n}$ yields:

$$\wp(\alpha_n) = \frac{1}{2\pi} \quad with \quad -\pi \leq \alpha_n \leq \pi \tag{5.16}$$

Finally, the phase angle $\psi_n$is also supposed to be uniformly distributed in the 2π range; that is:

$$\wp(\psi_n) = \frac{1}{2\pi} \quad with \quad -\pi \leq \psi_n \leq \pi \tag{5.17}$$

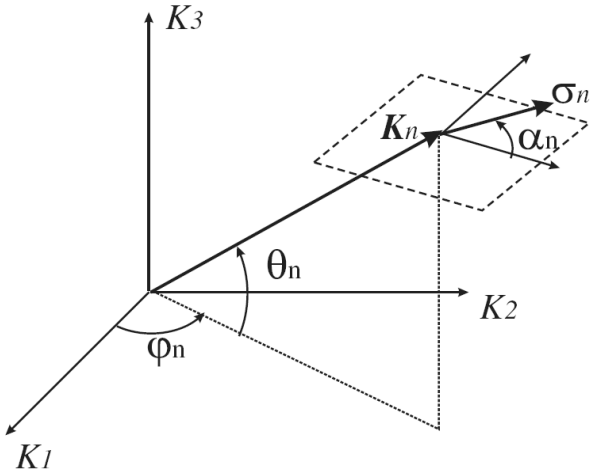

Figure 5.4 –Representation of the wave vector k_n and velocity direction vector σ_n, and definition of the stochastic angles.

The duration and sampling frequency of the synthetic velocity signals are defined on the basis of the prescribed minimum and maximum frequencies to be covered by the CAA analysis.

In particular, in order to prevent aliasing effects, the time step is such that twice the value of the prescribed maximum frequency can be achieved. Interestingly, a number of stochastic realizations of the source field can be computed by seeding the random generators. For each of them, the radiated noise is computed and results are finally averaged in order to track statistically converged noise spectra.

Additional details about the model are described by Casalino&Barbarino [8].

5.4. Agarwal approach

Consider the convective wave equation with a source term $\theta(\mathbf{x}, \mathrm{t})$ as reported in [35]:

$$\frac{D^2 p'}{Dt^2} - c_0^2 \nabla^2 p' = \rho c^2 \frac{D\theta}{Dt} \tag{5.18}$$

where $\frac{D}{Dt} = \frac{\partial}{\partial t} + \boldsymbol{u_0} \cdot \boldsymbol{\nabla}$. The Green's function for this convected wave equation satisfies:

$$\left(\frac{D^2}{Dt^2} - c_0^2 \nabla^2\right) G(\mathbf{x}, \mathrm{t}|\mathbf{x_q}, \mathrm{t}_q) = \delta(\mathbf{x} - \mathbf{x_q})\delta(t - t_q) \tag{5.19}$$

Once the Green's function for wave propagation and the noise source terms are known, the acoustic field p can be obtained by a straightforward convolution of the Green's function with the sources.

$$\mathrm{p}(\mathbf{x}, \mathrm{t}) = \rho c^2 \int_{V_q} \int_{-\infty}^{+\infty} G(\mathbf{x}, \mathrm{t}|\mathbf{x_q}, \mathrm{t}_q) \frac{D\theta(\mathbf{x_q}, t_q)}{Dt_q} dV_q dt_q \tag{5.20}$$

Where $\boldsymbol{x_q}$ indicates the source location, $\boldsymbol{x}$ the observer position, and c is the free-stream speed of sound. Applying the Fourier transform definition and introducing the frequency green function:

$$\mathrm{p}(\mathbf{x},\mathrm{t}) = \frac{\rho c^2}{2\pi}\int_{V_q} dV_q \int_{-\infty}^{+\infty} dt_q \int_{-\infty}^{+\infty} G_\omega(\mathbf{x}|\mathbf{x_q})\frac{D\theta(\mathbf{x_q},t_q)}{Dt_q} e^{-i\omega(t-t_q)}\, d\omega \qquad \textbf{(5.21)}$$

After some manipulation Agarwal achieved the following Spectral Density:

$$\mathrm{S}(\mathbf{x},\omega) = (\pi\omega\rho c^2)^2 A \int_{V_q} |G_\omega(\mathbf{x}|\mathbf{x_q})|\frac{m^4}{\tau_s} l_s^2 l_z\, e^{-\frac{\omega^2{\tau_s}^2}{4}} dV_q \qquad \textbf{(5.22)}$$

where:

$$l_s = c_l\frac{\sqrt{K_t}}{\Omega} \quad \tau_s = c_\tau\frac{1}{\Omega} \quad m = \frac{u_s}{\mathrm{c}} \quad u_s = \frac{\sqrt{2K_t}}{3} \qquad \textbf{(5.23)}$$

where l_s is the local turbulent length scale, τ_s is the turbulent timescale and A is the amplitude of the overall predicted noise spectrum at the source location.
The model includes also the constant l_z for the local turbulent length scale in spanwise direction. Since most standard turbulence models are isotropic l_z can be assumed equal to l_s.

The parameters K_t and Ω denote the turbulence kinetic energy and the specific dissipation rate obtained from a RANS model, whereas, c_l, c_τ and A are the empirical constants of the model that control the local turbulent length scale, l_s, the turbulent timescale, τ_s, at the source location and the amplitude of the overall predicted noise spectrum, A.

5.5. Trailing-edge noise prediction of a Naca0012 Airfoil

5.5.1. CFD results

CFD results carried out in the framework of the EU 7th Framework Clean Sky JTI ADOCHA Project and used in [8,24] are presented for a set of validation cases selected from the test report by Brooks et al. [25].

Emphasis is given to the boundary-layer quantities close to the trailing edge, since these are expected to have a major impact on the far-field noise spectra.

A NACA-0012 airfoil of chord c = 0.3048 m at a zero angle of attack and four values of the freestream velocity U have been considered: 31.7, 39.6, 55.5, and 71.3 m⁄s.

The turbulent transition is not triggered numerically, and the acoustic results are compared with the natural transition cases of [25].

Computations have been carried out using the CFD software Fluent by ANSYS. A pressure-based second-order upwind scheme has been employed to converge fully coupled RANS equations with turbulence accounted for through a $K-\omega$ SST model in transitional flow modality.

The turbulence level and length scale prescribed at the upstream boundary are 0.5% and 0.1 m, respectively.

A hybrid computational mesh has been used with a first cell spacing in the wall normal direction that provides a maximum y^+ distribution below the unitary value, thus ensuring a good resolution of the laminar sublayer.

The chordwise variation of the boundary-layer displacement thickness δ^*, momentum thickness θ, and wall skin friction τ_w have been extracted from the RANS solution.

Figure 5.5 shows a comparison between the predicted values of $\delta^*$and θ at 99.5% of the chord and the measurements made by Brooks et al.. The predicted values fall between the two sets of measurements, and the RANS results are very close to the untripped boundary-layer measurements.

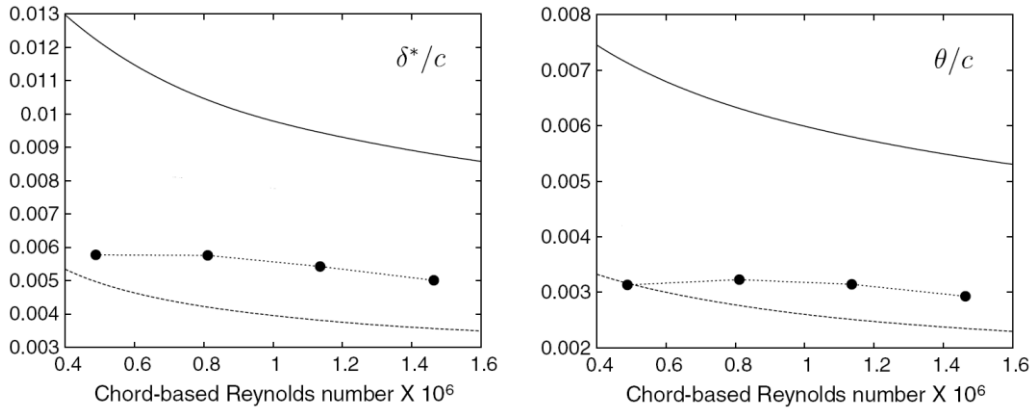

Figure 5.5 –NACA-0012 boundary-layer results at 99.5% of the chord. Comparison between experimental data, RANS solution (●). Measurements: tripped boundary layer (solid lines) and untripped boundary layer (dashed lines).

The RANS boundary-layer quantities at the trailing edge useful for the semi-analytical noise prediction are finally collected in Table 5.1.

U_a	U_e	$\delta \times 10^3$	$\delta^* \times 10^3$	$\theta \times 10^3$	τ_w	$dp_0/dx \times 10^5$
31.7	29.176	7.855	1.759	0.955	0.572	0.321
39.6	36.744	7.723	1.754	0.984	0.910	0.499
55.5	51.422	7.549	1.653	0.959	1.802	0.981
71.3	65.115	7.303	1.527	0.893	3.056	1.618

Table 5.1– NACA-0012 boundary-layer RANS results at 99.5% of the chord in SI units.

5.5.1. **Hybrid Empirical/FEM approach and analytical model**

To verify the hybrid approach described in Paragraph 5.2, the CIRA's FEM code solutions of the Howe's acoustic analogy equation [64] for a NACA-0012 airfoil are compared with analytical solutions for a zero-thickness airfoil obtained by using the formulation developed by Roger and Moreau (see equation (5.7))

The analytical solution uses the spanwise correlation length estimated using Corcos's equation (5.5).

The CIRA's FEM solution accounts for the 3D effects by using the formula proposed by Ewert et al. [39]. This formula accounts for both the propagation and generation effects by adding the quantity $10log(bLM/2\pi R)$ to the computed 2-D sound pressure levels, where b is an empirical spanwise correlation parameter that relates the spanwise correlation length to the freestream velocity and frequency, L is the

wingspan, R is the radiation distance, and M is the freestream Mach number. The parameter b is the same used in the Corcos's formula.

The boundary-layer quantities required by the wall-pressure spectrum model have been extracted from RANS solutions (Paragraph 5.5.1).

Figure 5.6 shows the comparison between the semi-analytical PSD noise results and the CIRA's FEM results. The agreement is very good at the four values of the freestream velocity. Also, the amplitude modulation due to the leading-edge backscattering is partially recovered by the CIRA's FEM solution, although the rounded edge of the airfoil tends to smear out the lobes. It can therefore be argued that modeling the trailing-edge noise generation from an airfoil through a wall-pressure fluctuation prescribed at the trailing edge provides numerical results that are in agreement with the classical Amiet's theory.

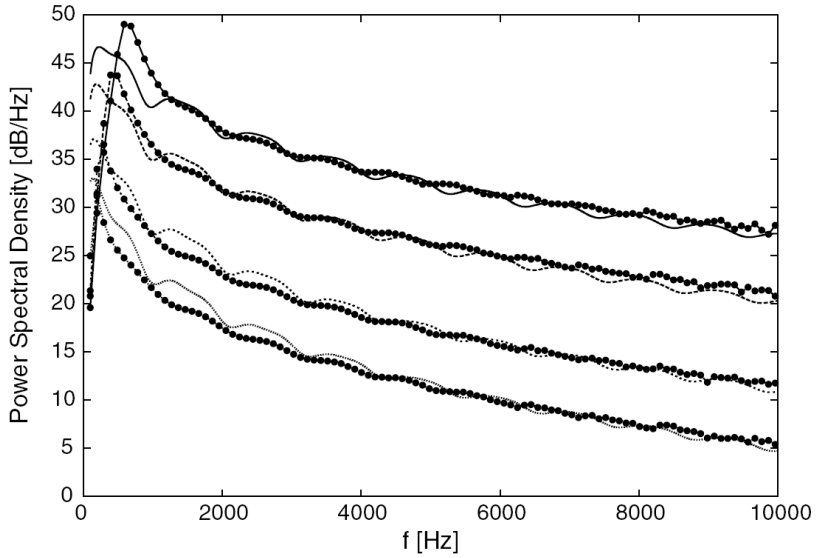

Figure 5.6 – NACA-0012 trailing-edge noise prediction. PSD computed using the Roger and Moreau's analytical formulation (lines) and the FEM solution of Howe's equation with a Dirichlet condition at the trailing edge (circles):U=71.3m/s (solid lines),U=55:5m/s (long dashed lines); U=39.6 m/s (medium dashed lines), and U=31.7m/s (short dashed lines).

5.5.2. **Stochastic Noise and Generation Model**

The SNGR approach has been tested in [8] by using the CIRA's FEM code OptydB as following described.

Computations have been carried out using the following values of the tuning parameters of the stochastic noise generation model: c_1=2.0, c_2=0.1, c_3=10, and c_4 =0.9 [8]. A number N_F = 100 of Fourier modes has been used.

A number of 25 realizations of the stochastic source fields have been computed in order to achieve an appropriate level of statistical convergence of the noise spectra.

The active source region is defined by prescribing a rectangular bounding box about the trailing edge that extends over 0.04 and 0.01 m along x and y, respectively (Figure 5.7).

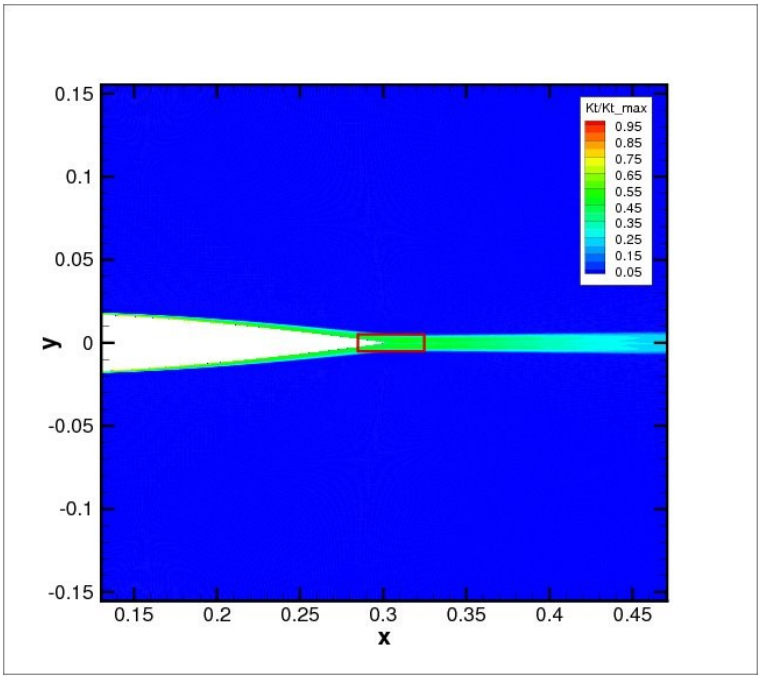

Figure 5.7 – Contour plot of the turbulent kinetic energy and bounding box extension.

Then, the cells of the CFD mesh have been filtered out at 1% of the maximum mean-flow velocity and 1% of the maximum turbulent kinetic energy in the source region. The resulting number of active source cells for the U=71.3 m/s case is 39.500. The size of the active source region has been determined by considering boxes of increasing size in both directions and by checking the convergence of the overall SPL (OASPL) at the 90 deg microphone for the higher freestream velocity case.

Figure 5.8 shows a comparison between the computed and the measured noise spectra in 1/3-octave bands for a microphone located at 90 deg with respect to the airfoil chord, at the same stream-wise location of the trailing edge, and at a radial distance of 1.22 m. The noise levels for the highest velocity case are over-predicted up to about 5 dB at the highest frequencies. Conversely, the low-frequency noise levels are under-predicted by about 5 dB for the lowest velocity case. Globally, the agreement between numerical predictions and measurements is fair.

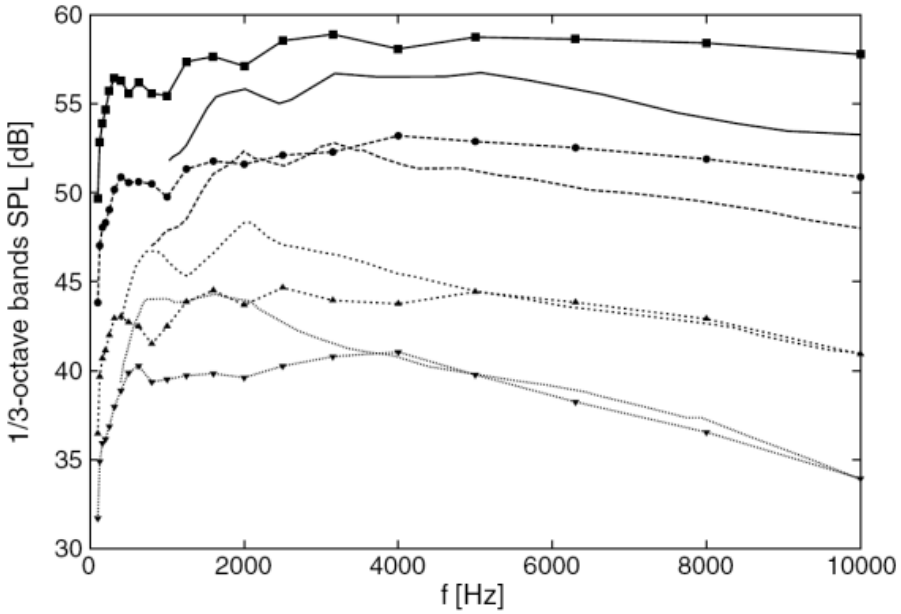

Figure 5.8 – Noise spectra in 1/3-octave bands at 90 deg for different free-stream velocities. Comparison between experimental data [25]. (lines) and numerical results (lines and symbols). Solid lines: U=71.3m/s, long-dashed lines: U= 55.5m/s, medium-length dashed lines: U=39.6m/s., and short-dashed lines: U=31.7m/s.

In addition, a verification process has been carried out by comparing the CAA results with semi-analytical results computed using boundary-layer quantities extracted from the same RANS solution used in the stochastic method (Figure 5.9). A good agreement has been observed at frequencies higher than about 4 kHz, which demonstrates the capability of the stochastic model to recover the two-point statistical properties of a wall-bounded turbulent flow-field.

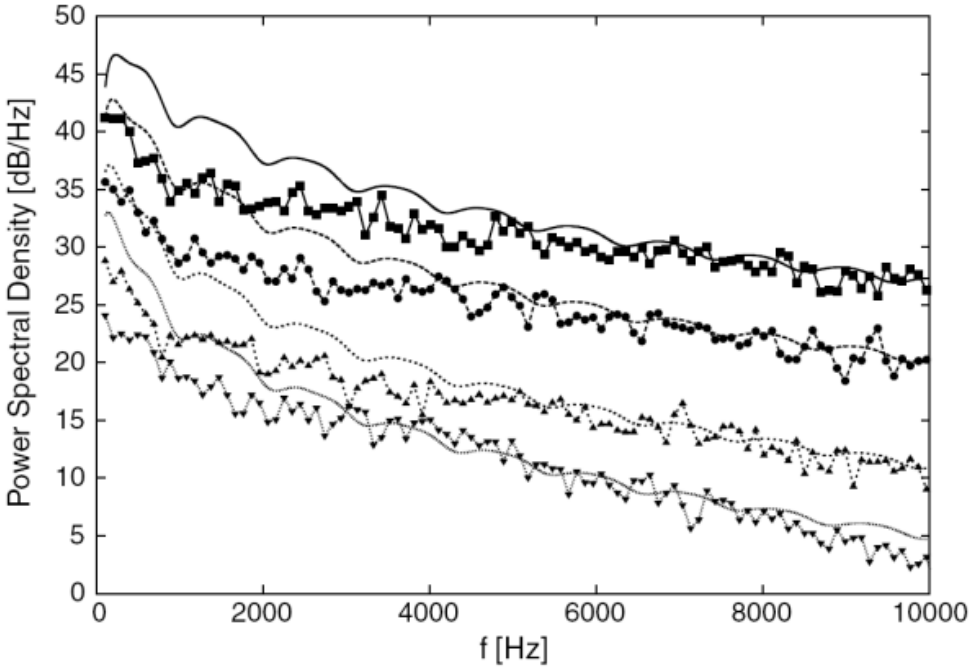

Figure 5.9 – Noise power spectral densities at 90 deg for different free-stream velocities. Comparison between semi-analytical (lines) and numerical results (lines and symbols). Solid lines: U=71.3m/s, long-dashed lines: U= 55.5m/s, medium-length dashed lines: U=39.6m/s., and short-dashed lines: U=31.7m/s.

5.5.3. **Agarwal model**

The Agarwal model has been tested by using the BEM model described and validated in Chapter 4.

Computations have been carried out using the following values of the tuning parameters of the Agarwal model: $c_l = 0.6$, $c_\tau = 1.8$ and $A = 0.7$.

The active source region is defined by prescribing a rectangular bounding box (*BB*) about the trailing edge as already illustrated in the Paragraph 5.5.1.

The bounding box technique consists in the generation of an automatic rectangular grid which extension and number of points is chosen by the user.

The active source region is selected by the *BB* extension and the CFD turbulent field is interpolated on the grid points of *BB*.

A convergence study of the source region is performed with the aim of investigating the effect of both bounding box extension and number of active source points. Three different bounding boxes have considered as illustrated in the Figure 5.10. The first one (*BB1*) extends over 0.04 and 0.01 m along *x* and *y*, respectively, the second one (*BB2*) over 0.08 and 0.03 m and the third one (*BB3*) over 0.31 and 0.06m. No CFD cells filters have been developed for this method.

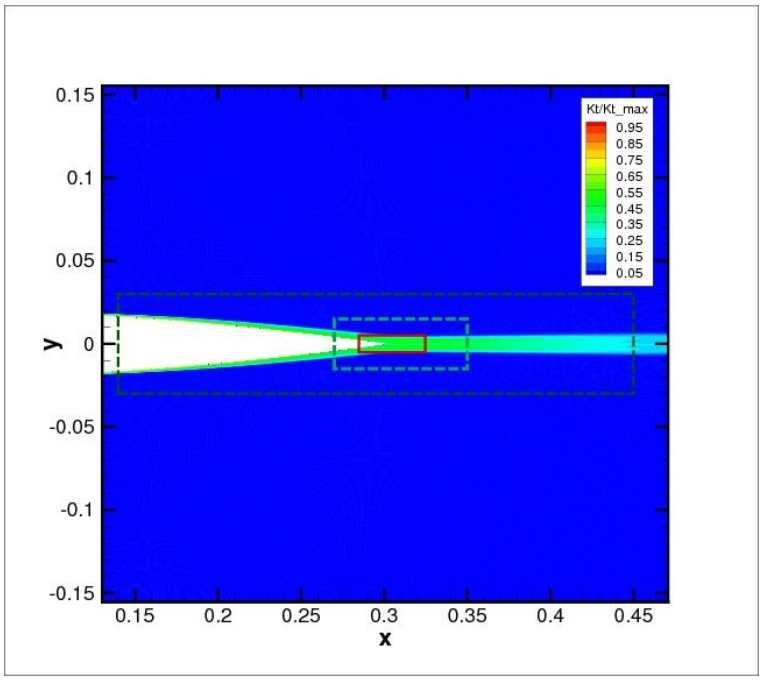

Figure 5.10 – Bounding boxes extension.

The first bounding box (*BB1*) has been tested for 400 and 10000 point sources whereas the second and third ones (*BB2* and *BB3*) only for 400 point sources.
Figure 5.11 shows a comparison between the computed and the measured noise spectra in 1/3-octave bands for a microphone located at 90 deg with respect to the airfoil chord, at the same stream-wise location of the trailing edge, and at a radial distance of 1.22 m.
The comparison between Figure 5.11a and Figure 5.11b shows that the influence of the source points number on the noise levels and curves shape is relatively low also increasing drastically the number of source points. On the contrary, by using the coarse grid points number (400 points) and the bounding box extensions *BB2* and *BB3*, noise levels increase significantly.

The noise levels for the highest velocity case are quite well predicted for the *BB3*. Levels at lower velocities are under-predicted especially for the lowest velocity case. This underestimation at lower velocities, even if of minor entity, is also partially noticed with the SNGR approach. This circumstance indicates that both RANS-based methods and CFD RANS solutions need further investigation.

Also the effect of CFD cells filters on the convergence of the method, against the bounding box extensions and source points number, need to be investigated.

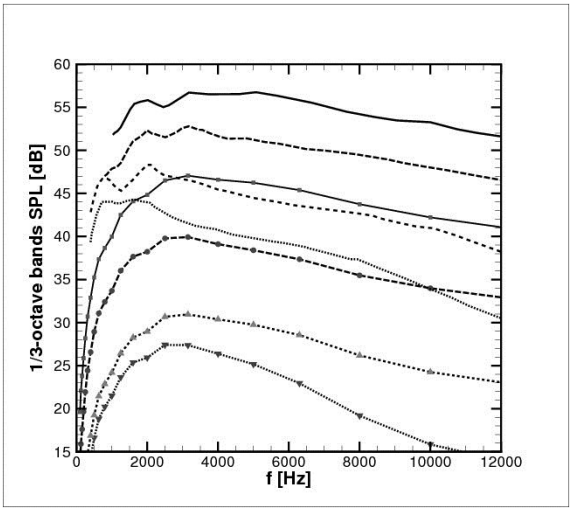

Figure 5.11a - BB1 with 10000 source points

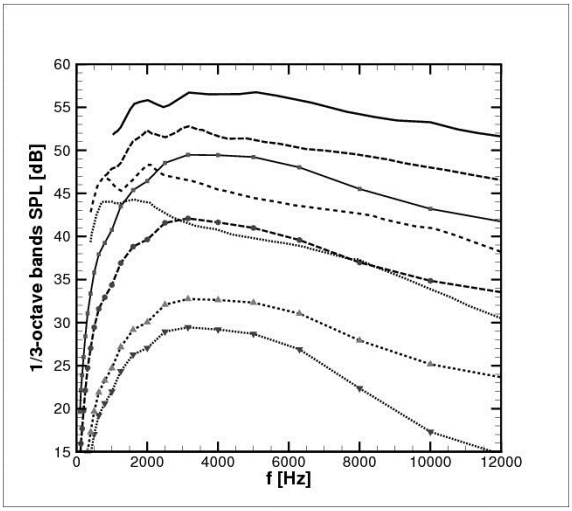

Figure 5.11b - BB1 with 400 source points

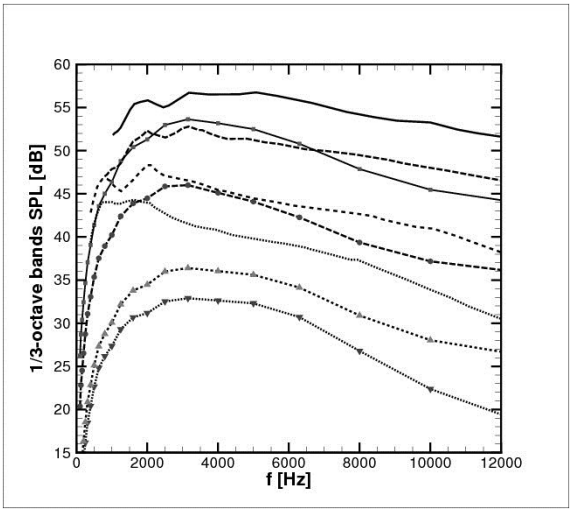

Figure 5.11c - BB2 with 400 source points

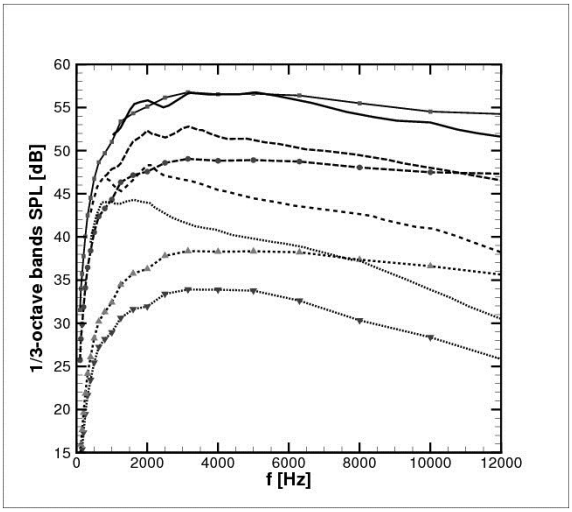

Figure 5.11d - BB3 with 400 source points

Figure 5.11 – Noise spectra in 1/3-octave bands at 90 deg for different free-stream velocities. Comparison between experimental data [25]. (lines) and numerical results (lines and symbols). Solid lines: U=71.3m/s, long-dashed lines: U= 55.5m/s, medium-length dashed lines: U=39.6m/s., and short-dashed lines: U=31.7m/s.

6. Preliminary Analyses for Low-Noise Design of a Landing Gear

6.1. Introduction

Landing gear noise is recognized to be one of the main sources for airframe noise, particularly on approach. Its prediction remains one of the most difficult challenges in aeroacoustics, because of the complexity of the gear geometry and the surrounding flow field.

In the context of the Clean Sky JTI – Green Regional Aircraft project, Landing Gear configurations were analyzed and acoustic design solutions for noise abatement were investigated.

In this Chapter the use of a wave equation analogy based on the approaches presented in the Paragraphs 4 (BEM) and 5 (RANS-based sources generation approach), for the preliminary design of low noise-devices is proposed.

This strategy for Landing Gear noise reduction is illustrated for a 2D Landing Gear model.

A CFD RANS solution (Paragraphs 5) or more simplified semi-empirical models [65] would allow generating noise sources. This aspect is out of the scope of the present Chapter, therefore, a fictitious point source is adopted as representative of the source field. This approach remains valid in general because the noise prediction can be achieved by means of the convolution approach once a source field is available.

Finally, the acoustic field scattering is predicted with the BEM tool and the use of an absorber material, as low-noise device, is also presented.

6.2. BEM analyses of a 2D Landing Gear model

A generic 3D configuration of a main landing gear installed on a mock-up fuselage, has been significantly simplified leading to two-dimensional sketched components, as depicted in Figure 6.1. The simplified two-dimensional model, however, is able to

represent the presence of the mock-up fuselage, the bay cavity, the main leg of the strut and the wheel.

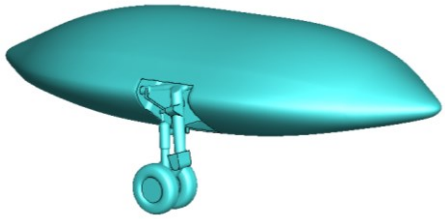

Figure 6.1a - 3D configuration

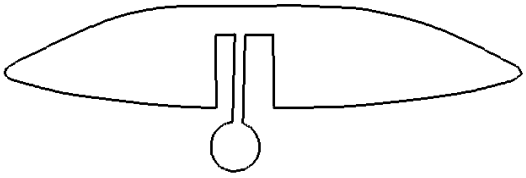

Figure 6.1b - 2D model

Figure 6.1 – 2D simplified Landing Gear configuration.

The flow field properties have been assumed to be c=342m/s and ρ=1.212kg/m^3. A grid mesh of 1142 segment elements has been generated.

A source point of unitary amplitude has been located downstream the wheel at *(5.25m,-1.5m)* as representative of the source region (Figure 6.2a)).

The BEM solution has been computed for both a microphones arc and a microphones grid (Figure 6.2). The microphones arc of 360 degree has been centered at the source location with a distance of 10m.

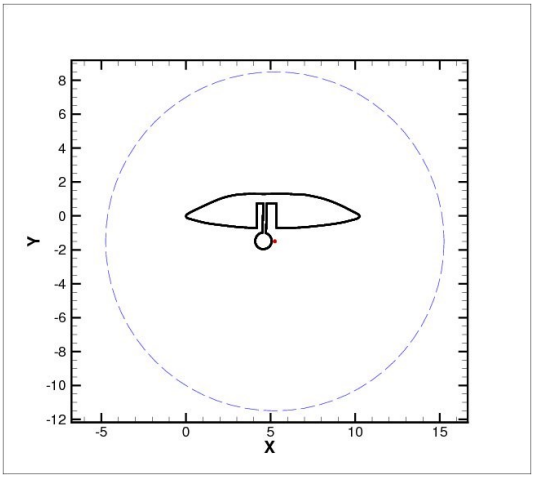

Figure 6.2a - Source location and microphones arc

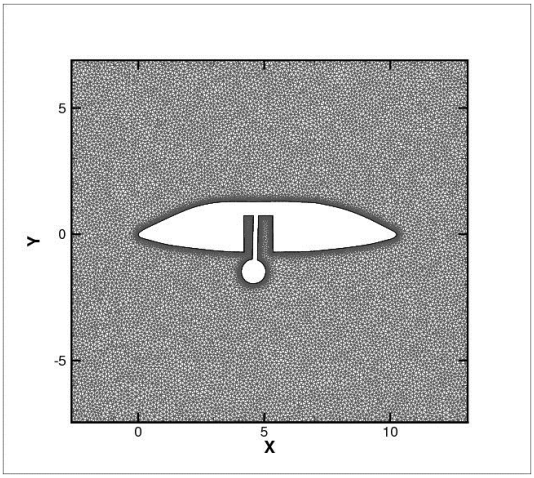

Figure 6.2b - Microphones grid

Figure 6.2 – Representation of the microphones arc and microphones grid.

Figure 6.3 shows plots of the real part of the acoustic pressure and directivity patterns in terms of SPL for four frequencies, respectively at 300, 500, 700, 1000 Hz.

Pictures underline the scattering effects of the sketched components at different frequency values.

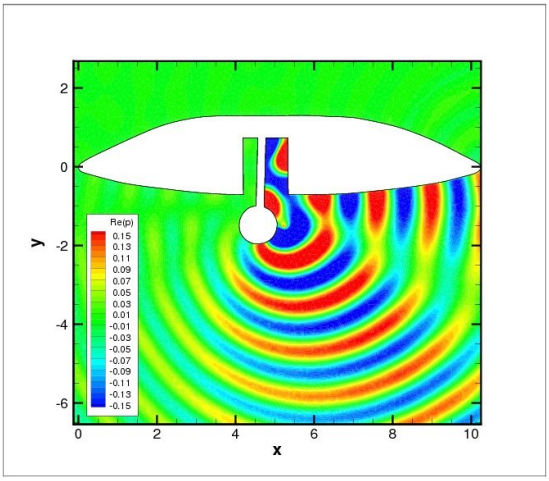

Figure 6.3a - Real part of the acoustic pressure at 300Hz

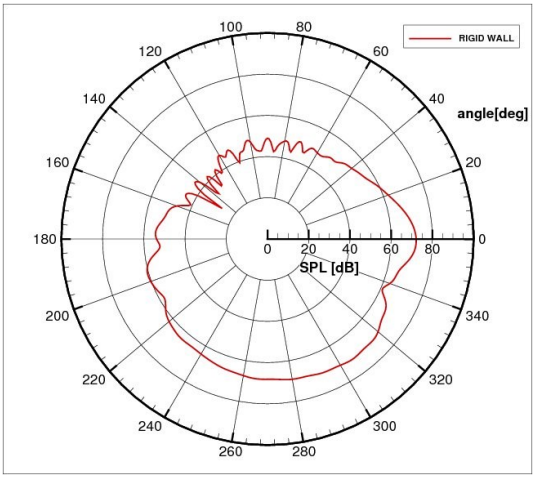

Figure 6.3b - SPL directivity pattern at 300Hz

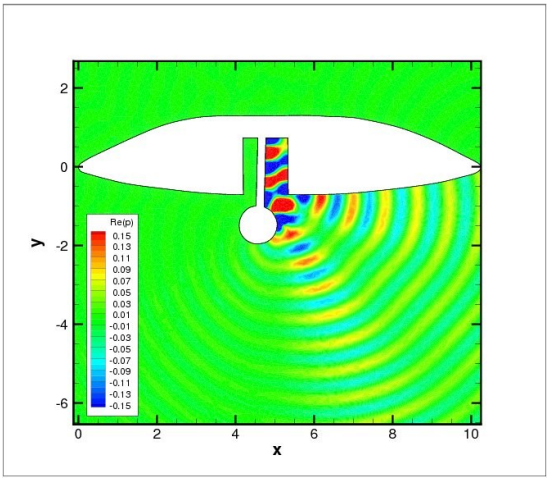

Figure 6.3c - Real part of the acoustic pressure at 500Hz

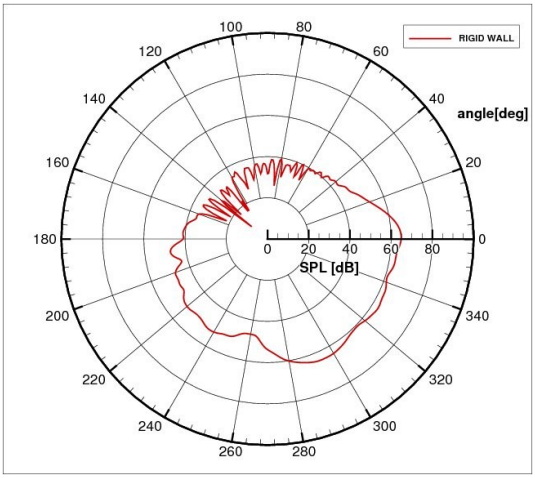

Figure 6.3d - SPL directivity pattern at 500Hz

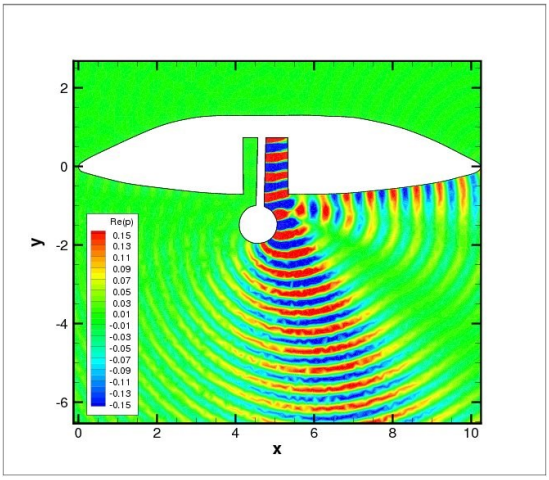

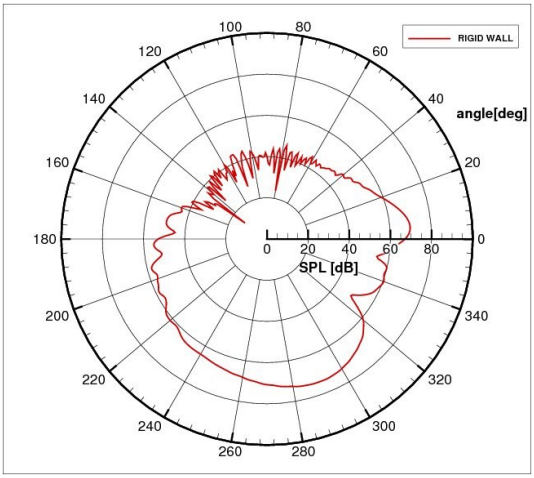

Figure 6.3e - Real part of the acoustic pressure at 700Hz

Figure 6.3f - SPL directivity pattern at 700Hz

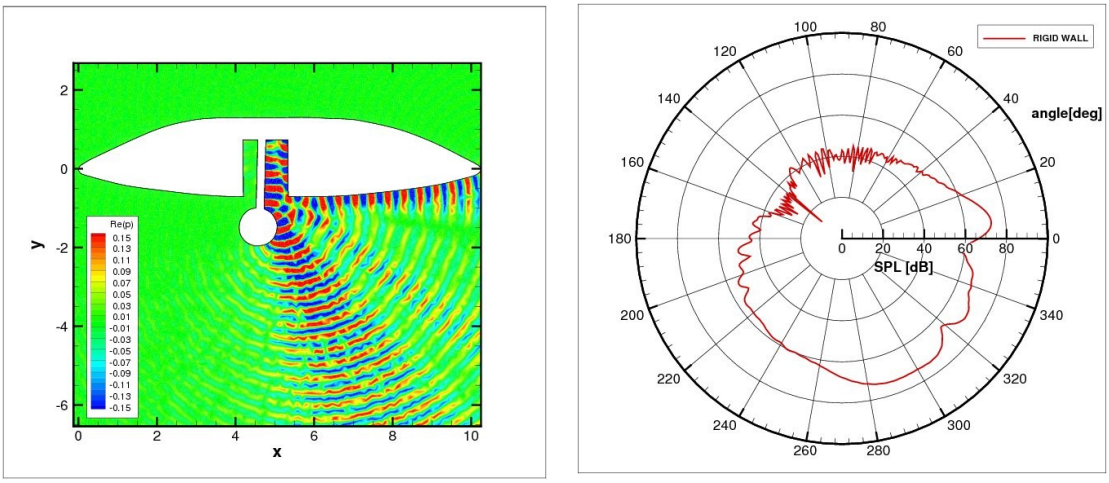

Figure 6.3g - Real part of the acoustic pressure at 1000Hz

Figure 6.3h - SPL directivity pattern at 1000Hz

Figure 6.3 – Contour plots of the acoustic pressure and directivity patterns in terms of SPL[dB]. Cavity modeled as rigid wall. Solutions at different frequencies.

The idea of applying an absorber material located in the cavity bay is illustrated. In order to investigate the effect of the absorber material, an impedance boundary condition has been applied in the cavity (Figure 6.4) with the characteristic impedance $Z = \rho c = 414.5$.

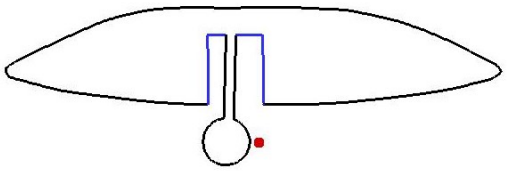

Figure 6.4 – Sketch of the impedance boundary condition applied in the cavity (blue line) and source point location (red dot).

Looking at the directivity patterns depicted in Figure 6.5, it appears the impedance produces a directivity changing and a substantial noise levels reduction except at 500Hz.

For this frequency, directivity exhibits a noise level increasing in the upstream direction combined with a reduction in the downstream direction, thus, noise global level appears slightly increased. This frequency has been further investigated increasing the CHIEF internal points up to 30%. No modifications for both

directivity and levels occur with the increased internal points. This behavior could be generated by a sort of bay cavity resonance at that frequency and it requires to be further investigated.

The design and optimization of a liner device to be applied as absorber in the cavity can be performed with the use of semi-empirical models as already showed by Casalino&Barbarino [24]. These models allow estimating the liner impedance from the knowledge of liner manufacturing parameters.

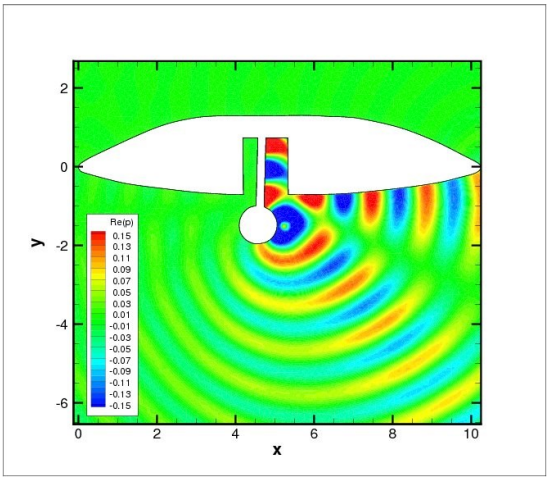

Figure 6.5a - Real part of the acoustic pressure at 300Hz

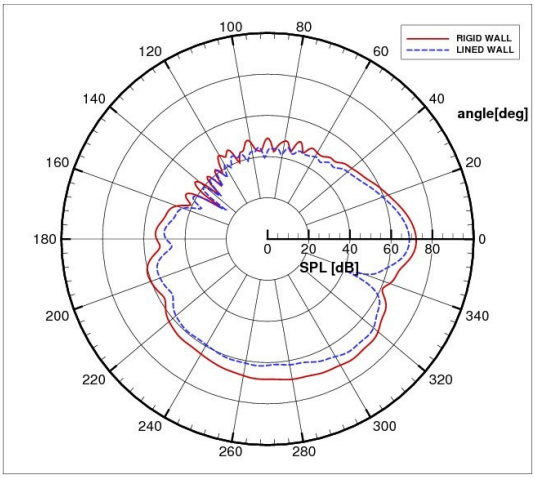

Figure 6.5b - SPL directivity pattern at 300Hz

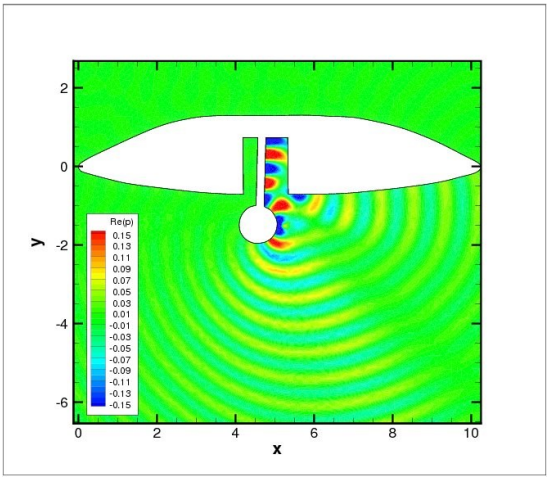

Figure 6.5c - Real part of the acoustic pressure at 500Hz

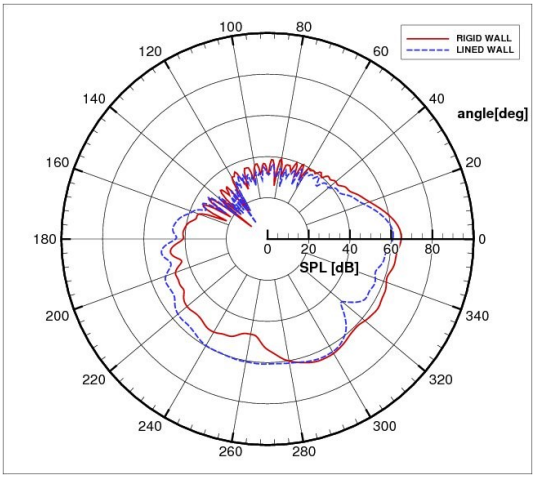

Figure 6.5d - SPL directivity pattern at 500Hz

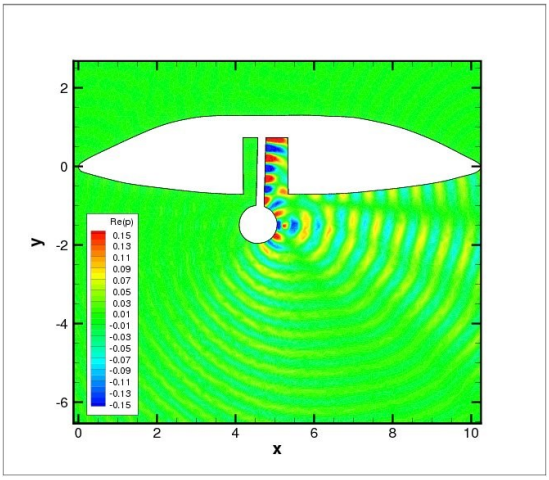

Figure 6.5e - Real part of the acoustic pressure at 700Hz

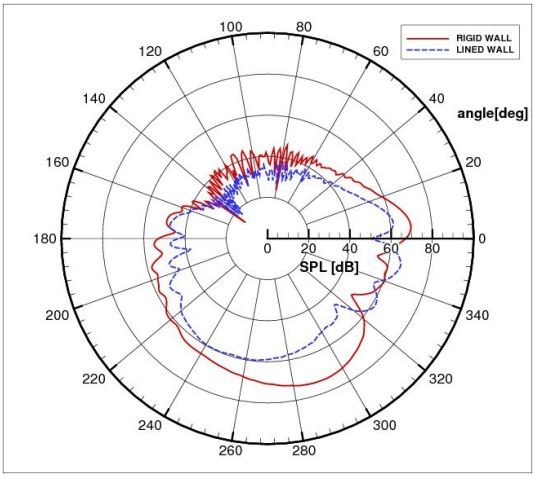

Figure 6.5f - SPL directivity pattern at 700Hz

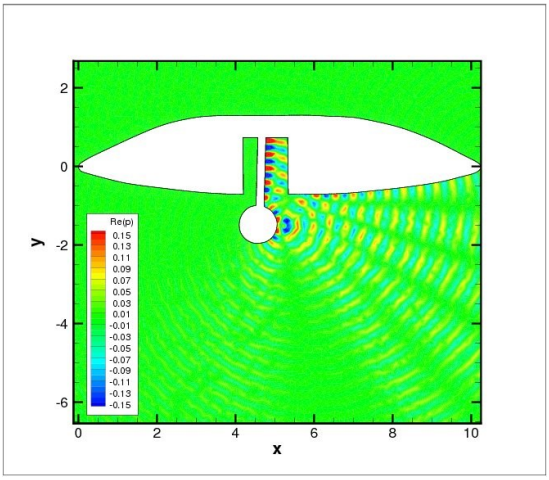

Figure 6.5g - Real part of the acoustic pressure at 1000Hz

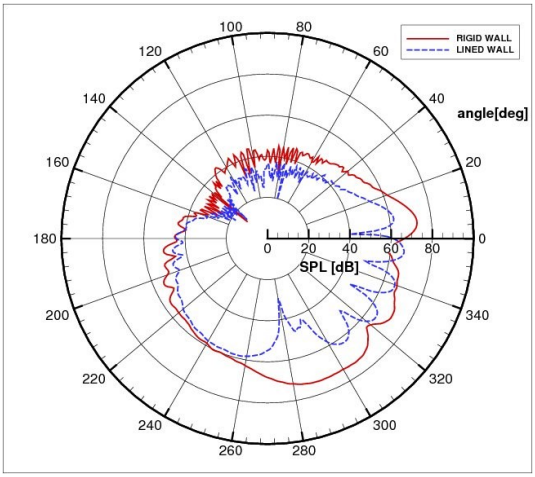

Figure 6.5h - SPL directivity pattern at 1000Hz

Figure 6.5 – Contour plots of the acoustic pressure and directivity patterns in terms of SPL[dB]. Cavity modeled as treated wall. Comparison between rigid wall (red continuous lines) and (blue dashed lines). Solutions at different frequencies.

Liner consists of a single-layer sandwich with a solid backplate, a perforated facesheet and a honeycomb core as depicted in Figure 6.6a. The concept can be extended to a 2-DOF liner by simply adding a second layer of honeycomb separated by a porous septum, as sketched in Figure 6.6b.

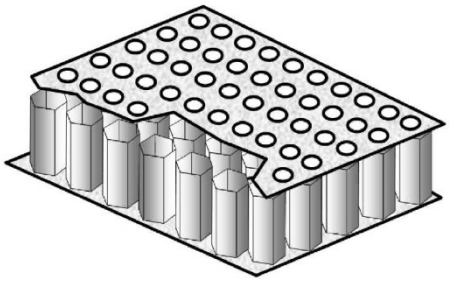

Figure 6.6a - 1 DoF

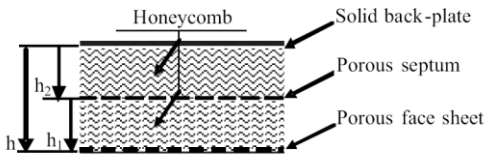

Figure 6.6b - 2 DoF

Figure 6.6 – Illustration of 1-DOF and 2-DOF liners.

Compared with a 1-DOF treatment, a 2-DOF treatment is effective on a wider frequency range. Since the noise generated by the Landing Gear is broadband in nature, a 2-DOF liner is expected to be more appropriate for broadband noise problems as showed by Casalino&Barbarino [24]. The general impedance formula for a 1-DOF liner [66] reads:

$$\hat{Z} = R + i(\chi_m + \chi_c) \tag{6.1}$$

Where R is the porous-surface resistance, $\chi_m$is the porous-surface mass reactance and χ_c is the cavity reactance that reads:

$$\chi_c = -\cot(kh) \tag{6.2}$$

where h is the cavity depth (honeycomb thickness). In line with the typical assumption made in the literature, the $+i\omega t$ convention is used for the definition of the impedance. It is very important underline that, as illustrated in the Paragraph 4.4.1, BEM method has been implemented with the $-i\omega t$ convention. Therefore is straightforward that the complex conjugate of impedance computed according to the procedure illustrated in this paragraph should be used in the BEM computation.

The resistance term results from three distinct contributions: two linear contributions due to the energy loss across the orifices and in the facesheet boundary layer in the presence of grazing flow, and one nonlinear contribution due to the microjet from the orifice induced by the pressure wave and thus proportional to the magnitude of the

acoustic velocity fluctuation. The theoretical and experimental characterization of these effects is the objective of an important research area, but the simple choice of selecting the models reported in [66] is made. Moreover, the nonlinear contribution can neglected, supposing that the noise acoustic levels are not high enough to induce nonlinear energy losses. Hence, the facesheet and septum resistance and mass reactance are estimated using the following formulas:

$$\chi_c = \frac{64\mu\tau}{2\rho c\varrho C_d d^2} + \frac{M_e}{\varrho\left(2 + 1.256\frac{\delta^*}{d}\right)}$$

$$\chi_m = \frac{k\left[\tau + 0.85d(1 - 0.7\sqrt{\varrho})/(1 + 305M_e^3)\right]}{\varrho} \quad \textbf{(6.3)}$$

where τ is the porous-surface thickness, μ is the fluid viscosity, d is the orifice diameter, C_d is a non-dimensional orifice discharge coefficient due to the contraction of the flow passage section across the orifice, δ^* is the boundary-layer displacement thickness, M_e is the boundary-layer asymptotic Mach number, and $\varrho = N_s\pi d^2/4$ is the surface porosity defined as the ratio between the orifices area and the total area, N_s being the number of orifices for unit surface. A typical value of $C_d$is 0.76. Of course, the septum resistance and mass reactance are estimated by setting $M_e = 0$ in the formulas.

Figure 6.7 shows the typical shape of the Admittance, $\hat{A} = 1/\hat{Z}$ achieved by applying the equation (6.3) with the following flow conditions:

$$\rho = 1.225kg/m^3 \quad c = 340m/s \quad \mu = 1.8025 \cdot 10^{-5} \quad M_e = 0$$

and where the following parameters are also assumed by the current manufacturing practices:

$$\varrho = 0.12 \quad C_d = 0.76$$
$$h = 0.15m \quad \tau = 0.002m \quad d = 0.0005m$$

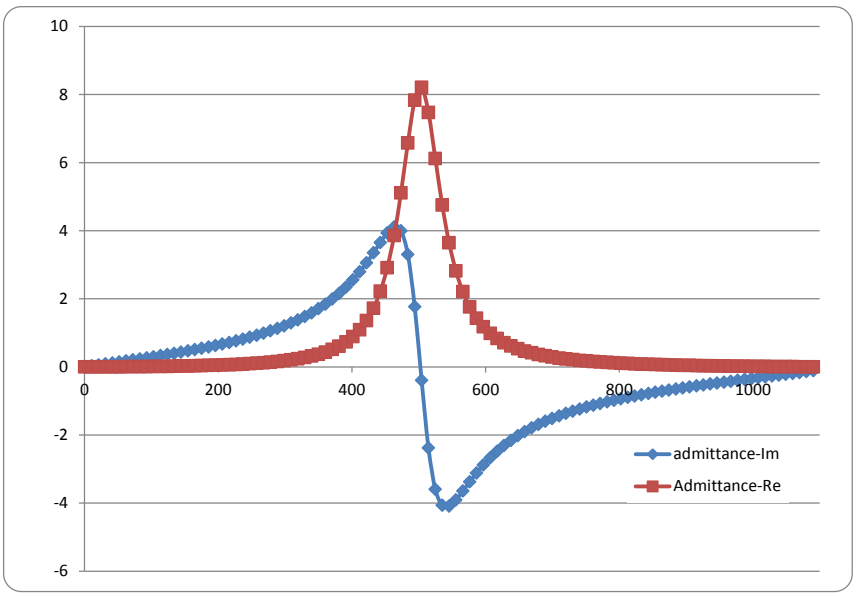

Figure 6.7 –Liner impedance performance computed with Motsinger&Kraft model [66].

Following the described approach, once the Green functions of the configuration with the acoustic device are computed for all the frequency range of interest and for all the source points characterizing the source region, the convolution approach would allow the noise prediction by means of RANS-based models (Paragraph 5) or more simplified semi-empirical models [65].

7. Conclusions

The present dissertation has focused on the development and validation of aeroacoustic methodologies able to address the aeroacoustic design of aeronautical low-noise technologies in an industrial context.

The thesis starts with the theoretical formulation of the Acoustic Analogy approach based on the Lighthill's equation (Chapter 3). Particular attention has been devoted to the convected Lighthill's wave equation for uniform mean flow and the corresponding homogeneous wave equation in frequency domain. The analytical solution of the free-field Green function has also been presented.

Chapter 4 describes the main aspects of the Boundary Element Method (BEM) technique. The BEM approach has been used to solve the convected Helmholtz wave equation for uniform mean flow.
The BEM approach has been implemented in order to manage hybrid unstructured grids treating segment, triangular and quadrilateral elements. The normal vector direction of each panel is managed with a semi-automatic procedure only for single-connected domains by specifying an internal point of the domain and the type of simulation (internal or external problem). However, for multi-connected domains a post-processing file is generated for checking the right direction of the normal vectors.
The BEM approach builds up the global system matrix by assembling different matrix blocks for the governing equations and the boundary conditions. This strategy allows a more general and efficient implementation of the boundary conditions.
Also a sufficiently large set of boundary conditions, for internal and external problems, has been implemented. Numerical instabilities for external problems are also avoided through the CHIEF method. The CHIEF kernel generates in a random way the needed internal points once the user has previously defined bounding boxes where collocate the points.
Furthermore, classical analytical test cases for both internal and external problems has been also presented and used for the BEM approach validation. Comparisons

between numerical and analytical results have underlined the correct implementation of the method. Moreover, the comparison with the CIRA's FEM code accounting for the non-uniform mean flow has been shown that the BEM approach provides good results for relatively low-Mach number flows.

In Chapter 5 attention has been given to the broadband noise mechanism generated by aeronautical devices (called Airframe noise).
After an overview of the best known semi-empirical and RANS-based approaches about the turbulent source field generation, the attention was devoted to some of them.
The first approach to be presented concerns the use of semi-empirical wall pressure spectra in proximity of edges to be used as a Dirichlet boundary condition of a FEM or BEM problem. This semi-empirical model, being a function of the boundary layer variables, allows a direct connection to CFD RANS solutions.
The approach has been applied to the self-noise prediction of a NACA0012 airfoil by using CIRA's FEM code. The comparison with the semi-analytical model showed that modeling the trailing-edge noise generation from an airfoil through a prescribed wall-pressure fluctuation at the trailing edge provides numerical results that are in agreement with Amiet's classical theory.
The second approach concerns an extension of the SNGR approach recently developed by Casalino&Barbarino. This method has also been applied to the self-noise prediction of a NACA0012 airfoil by using the CIRA's FEM code at four different Mach numbers. The comparison with experimental results show that noise levels for the highest velocity case are over-predicted up to about 5 dB at the highest frequencies. Conversely, the low-frequency noise levels are under-predicted by about 5 dB for the lowest velocity case.
The third approach concerns the statistical RANS-based model developed by Agarwal and its application with the BEM solver. After a converge study of the source region, both poor and fair results have been achieved in comparisons with experimental data. In particular, the highest velocity has appeared quite well predicted, conversely the lowest velocities have been considerably underestimated.

This underestimation at lower velocities, even if of minor entity, is also partially noticed with the SNGR approach. This circumstance indicates that both RANS-based methods and CFD RANS solutions need further investigation.

Finally in Chapter 6 the application of the BEM method to the analysis of the Landing Gear low-noise design problem is presented. The case study has been presented as one of the possible aircraft component to be investigated for the airframe noise reduction. In particular, the application of absorber materials in the bay cavity of the landing gear as acoustic low-noise device has been also investigated. Furthermore, a possible bay cavity resonance at a certain frequency seemed to appear. This last aspect requires further investigations.

The present dissertation demonstrates that, in spite of the complexity of the aeroacoustic phenomena, different effective methods can be developed for the design of low noise technologies. Simplified approaches, such as those based on the acoustic analogy, are in particular effective in predicting noise during preliminary design and optimization studies, above all for complex configuration of industrial interest.

Concerning the BEM approach, it has been demonstrated that it allows predicting acoustic scattering in uniform mean flow in an efficient way.
Despite BEM allows an extensive simplification of the grid generation phase, it produces a dense system matrix that is highly demanding in terms of memory requirements and computing time for complex industrial configurations. However, Fast Multipole Methods developed in recent years and applied to the BEM approach allows to overcome these limits.

Concerning RANS-based methods, it has been shown that they require both an accurate calibration of the model parameters and a careful use of RANS CFD solutions especially in regards to the turbulence models. Even if the results obtained with these approaches didn't provide a perfect overlapping with the experimental data, the outcomes are however encouraging. RANS-based methods remain

promising methodologies for design and optimization phases to be further investigated.

More computationally demanding approaches like LES, DES or DNS certainly remains the state of art in order to investigate complex noise generation mechanisms especially in flow conditions for which the separation between the acoustic propagation field and turbulent flow field is not an appropriate simplification.

Bibliography

1 Web-site, "*Air Transport Action Group*", http://www.atag.org/facts-and-figures.html.

2 Lighthill, M., J., "*On sound generated aerodynamically: I. general theory*", Proceedings of the Royal Society of London, Series A: Mathematical and Physical Sciences, Vol. 211, 1952, pp. 564-587.

3 Lighthill, M., J., "*On sound generated aerodynamically: II. turbulence as source of sound*", Proceedings of the Royal Society of London, Series A: Mathematical and Physical Sciences, Vol. 222, 1954, pp. 1-32.

4 Ffowcs Williams, J. E. and Hawkings, D. L., "*Sound Generated by Turbulence and Surfaces in Arbitrary Motion*", Philosophical Transactions of the Royal Society, Vol. A264, No. 1151, 1969, pp.321-342.

5 Rienstra, S.,W., Hirschberg, A., "*An Introduction to Acoustics",* Eindhoven University of Technology, 19 July 2006.

6 Goldstein, M., E., "*Aeroacoustics*", McGraw-Hill Book Company, Inc., New York, 1976.

7 Pierce, A., D., "*Acoustics: an Introduction to its Physical Principles and Applications*", McGraw-Hill Book Company, Inc., New York, 1981.

8 Casalino, D., Barbarino, M., "*Stochastic Method for Airfoil Self-Noise Computation in Frequency-Domain*", AIAA Journal, Vol. 49, No. 11, 2011, pp. 2453-2469.

9 Hetsch, T, Preisser, D., Forsey, C.,Smith, M., "*ADOCHA: Acoustic noise prediction for high-lift configurations*", Clean Sky JTI-GRA Report (not for public domain), 2010.

10 STS, "*An introduction to Boundary Element Methods for Acoustics*", VNoise Technical Manual, 2003.

11 Marburg, S., Nolte, B., "*Computational Acoustics of Noise Propagation in Fluids – Finite and Boundary Element Methods*", Springer, 2008.

12 Casalino, D., Barbarino, M., Visingardi, A., "*Simulation of Helicopter Community Noise in Complex Urban Geometry*", AIAA Journal, Vol. 49, No. 8, 2011, pp. 1614-1624.

13 Lee, S., Brentner, K., Morris, P.,J., "*Time Domain Approach for Acoustic Scattering of Rotorcraft Noise*", Journal of American Helicopter Society, Vol. 57, No. 4, 2012 , pp. 1-12.

14 Casalino, D., "*An advanced time approach for acoustic analogy predictions*", JSV, Vol. 261, 2003, pp. 583-612.

15 Schenck, H., A, "*Improved integral formulation for acoustic radiation problems*", J. Acoust. Soc. Am., Vol. 44, 1968.

16 Seybert, A.,F., Wu, T.,W., "*A weighted residual formulation for the chief method in acoustic",* J. Acoust. Soc. Am., Vol. 90, 1991.

17 Segalman, D., J., Lobitz, D.,W., "*A method to overcome computational difficulties in the exterior acoustic problem"*, J. Acoust. Soc. Am., Vol. 91, 1992.

18 Darve, E., "*The Fast Multipole Method: Numerical Implementation, Journal of Computational Physics*" Vol. 160, 2000, pp. 195–240.

19 Darrigrand, E., "*Coupling of Fast Multipole Method and Microlocal Discretization for the 3-D Helmholtz Equation*", Journal of Computational Physics, Vol. 181, 2002, pp. 126–154.

20 Fong, W., Darve, E., "*The black-box fast multipole method*", Journal of Computational Physics, Vol. 228, 2009, pp. 8712–8725.

21 Morse, P., M., Ingard, K., U., "*Theoretical Acoustics McGraw-Hill*", 1968.

22 Crighton, D., G., Dowling, A., P., Ffowcs Williams, J., E., Heckl, M., and Leppington, F.,G., "*Modern Methods in Analytical Acoustics: Lecture Notes"*, Springer-Verlag, London, 1992.

23 Tsuji, T., Tsuchiya, T., and Kagawa, Y., "*Finite Element and Boundary Element Modelling for the Acoustic Wave Transmission in mean flow medium*," Journal of Sound and Vibration, Vol. 255, No. 5, 2002, pp. 849–866.

24 Casalino, D., Barbarino, M., "*Optimization of a Single Slotted Lined Flap for Wing Trailing Edge Noise Reduction*", AIAA Journal of Aircraft, Vol. 49, No. 4, 2012.

25 Brooks, T., Pope, D., and Marcolini, M., "*Airfoil Self-Noise and Prediction*", NASATR 1218, 1989.

26 Guo, Y., "*Aircraft Flap Side Edge Noise Modeling and Prediction*", AIAA Paper 2011-2731, 2011.

27 Terracol, M., Labourasse, E., Manoha, E., and Sagaut, P., "*Simulation of the 3-D Unsteady Flow in a Slat Cove for Noise Prediction*", AIAA Paper 2003-3110, May 2003.

28 Deck, S., "*Zonal-Detached-Eddy Simulation of the Flow Around a High-Lift Configuration*", AIAA Journal, Vol. 43, No. 11, 2005, pp. 2372–2384.

29 Marsden, O., Bailly, C., and Bogey, C., "*Direct Noise Computation of the Turbulent Flow Around a Zero-Incidence Airfoil*", AIAA Journal, Vol. 46, No. 4, 2008, pp. 874–883.

30 Waller,G. C., "*Prediction of Flap-Edge Noise Using STAR-CD*", AIAA Paper 2008-2863, May 2008.

31 König, D., Koh, S. R., Schröder, W., and Meinke, M., "*Slat Noise Source Identification*", AIAA Paper 2009-3100, May 2009.

32 Langtry, R. B., Gren, E. A., Larssen, J. V., and Spalart, P. R., "*Evaluation of Structured and Unstructured Grids for Detached Eddy Simulation of Flap Edge Noise*", AIAA Paper 2009-3102, May 2009.

33 Ma, Z., and Zhang, X., "*Numerical Investigation of Broadband Slat Noise Attenuation with Acoustic Liner Treatment*", AIAA Journal, Vol. 47, No. 12, 2009, pp. 2812–2820.

34 Hosder, S., Schetz, J., Grossman, B., and Mason, W., "*Airframe Noise Modeling Appropriate for Multidisciplinary Design and Optimization*", AIAA Paper 2004-0698, Jan. 2004.

35 Agarwall, A., Morris, P., J., "*Prediction Method for Broadband Noise*", AIAA Journal, Vol. 44, No2, February, 2006.

36 Agarwall, A., "*The Prediction of Tonal and Broadband Slat Noise*", PhD Thesis, The Pennsylvania State University, May 2004.

37 Casalino, D., Barbarino, M., Genito, M., Ferrara, V., "*Hybrid Empirical/Computational Aeroacoustics Methodology for Rocket Noise Modeling*", AIAA Journal, Vol. 47, No. 6, 2009.

38 Ewert, R., "*CAA Slat Noise Studies Applying Stochastic Sound Sources Based On Solenoidal Digital Filters*", AIAA Paper 2005-2862, May 2005.

39 Ewert, R., Appel, C., Dierke, J., and Herr, M., "*RANS/CAA Based Prediction of NACA 0012 Broad-band Trailing Edge Noise and Experimental Validation*", AIAA Paper 2009-3269, May 2009.

40 Morris, P., J., Farassat, F., "*Acoustic Analogy and Alternative Theories for Jet Noise Prediction*", Vol. 40, 2002, pp. 671-680.

41 Tam, C., K., W., Auriault, L., "*Jet Mixing Noise from Fine-Scale Turbulence*", AIAA Journal, Vol. 37, 1999, pp.145-153.

42 Kraichnan, R., H., "*Diffusion by a Random Velocity Field*", Physics of Fluids, Vol. 13, No. 1, 1970, pp. 22–31.

43 Fung, J., C., H., Hunt, J., C., R., Malik, N., A., and Perkins, R., J., "*Kinematic Simulation of Homogeneous Turbulence by Unsteady Random Fourier Modes*", Journal of Fluid Mechanics, Vol. 236, 1992, pp. 281–318.

44 Béchara,W., Bailly, C., Lafon, P., and Candel, S., "*Stochastic Approach to Noise Modeling for Free Turbulent Flows*", AIAA Journal, Vol. 32, No. 3, 1994, pp. 455–464.

45 Bailly, C., and Juvé, D., "*A Stochastic Approach to Compute Subsonic Noise Using Linearized Euler's Equations*", AIAA Paper 1999-1872, May 1999.

46 Billson, M., Eriksson, L., and Davidson, L., "*Jet Noise Modeling Using Synthetic Anisotropic Turbulence*," AIAA Paper 2004-3028, 2004.

47 Amiet, R., K., "*Acoustic radiation from an airfoil in a turbulent stream*", J. Sound Vib.,41(4), p. 407-420, 1975.

48 Paterson, R. W. and Amiet, R. K., "*Acoustic radiation and surface pressure characteristics of an airfoil due to incident turbulence*", NASA CR-2733, September 1976.

49 Roger, M. and Moreau, S., "*Bach-Scattering Correction and Further Extensions of Amiet's Trailing Edge Noise Model, Part 1: Theory*", Journal of Sound and Vibration, Vol. 286, No. 3, 2005, pp. 477–506.

50 Moreau, S. and Roger, M., "*Competing Broadband Noise Mechanisms in Low-Speed Axial Fans*", AIAA Journal, Vol. 45, No. 1, 2007, pp. 48–57.

51 Blandeau, V. and Joseph, P., "*Broadband Noise Due to Rotor-Wake/Rotor Interaction in Contra-Rotating Open Rotors*", AIAA Journal, Vol. 48, No. 11, 2010, pp. 2674–2686.

52 Blandeau, V. and Joseph, P., "*On the Validity of Amiet's Model for Propeller Trailing-Edge Noise*", AIAA Paper 2010–3797, June 2010.

53 Schlinker, R. H. and Amiet, R. K., "*Helicopter Rotor Trailing Edge Noise*", NASA CR-3470, 1981.

54 Pagano, A., Barbarino, M., Casalino, D., and Federico, L., "*Tonal and Broadband Noise Calculations for Aeroacoustic Optimization of a Pusher Propeller*", AIAA Journal of Aircraft, Vol. 47, No. 3, 2010.

55 Chase, D. M., "*Modeling the Wavevector-Frequency Spectrum of Turbulent Boundary Layer Wall Pressure*", Journal of Sound and Vibration, Vol. 70, No. 1, 1980, pp. 29–67.

56 Goody, M., "*Empirical Spectral Model of Surface Pressure Fluctuations*", AIAA Journal, Vol. 42, No. 9, 2004, pp. 1788–1794.

57 Rozenberg, Y., "*Modélisation Analytique du Bruit Aérodynamique à Large Bande des Machines Tournantes: Utilisation de Calculs Moyennés de Mécanique des Fluides*," Ph.D. thesis, Ecole Centrale de Lyon, Dec. 2007.

58 Willmarth, W. W., and Roos, F., "*Resolution and Structure of the Wall Pressure Field Beneath a Turbulent Boundary Layer*", Journal of Fluid Mechanics, Vol. 22, 1965, pp. 81–94.

59 Casper, J. and Farassat, F., "*A new time domain formulation for broadband noise predictions*", International Journal of Aeroacoustics, Vol. 1. No. 3, 2002, pp. 207-240.

60 Casper, J. and Farassat, F., "*Trailing Edge Noise Prediction Based on a New Acoustic Formulation*", In Proceedings of the 8th AIAA/CEAS Aeroacoustics Conference and Exhibits, Breckenridge, CO, Nevada, USA, AIAA-2002-2477, June 2002.

61 Casper, J. and Farassat, F., Mish, P., F., Devenport, W., J., "*Broadband Noise Predictions for an Airfoil in a Turbulent Stream*", In Proceedings of the 41st Aerospace Sciences Meeting & Exhibit, Reno, Nevada, USA, AIAA-2002-0366, January 2002.

62 Casper, J. and Farassat, F., "*Broadband Trailing edge noise predictions in the time domain*", J. Sound Vib., 271, pp. 159-176, 2004.

63 Barbarino, M., Casalino, D., "*Hybrid Analytical/Numerical Prediction of Propeller Broadband Noise in the Time Domain*", International Journal of Aeroacoustics, Vol. 11, No.2 , 2012, pp. 157-176.

64 Howe, M. S., "*Contributions to the Theory of Aerodynamic Sound, with Application to Excess Jet Noise and the Theory of the Flute*," Journal of Fluid Mechanics, Vol. 71, 1975, pp. 625–673.

65 Guo, Y.,P., Yamamoto, K., J., Stoker, R., W., "*An empirical model for Landing Gear Noise prediction"*, 10th AIAA/CEAS Aeroacoustics conference, AIAA 2004-2888, 2004.

66 Motsinger, R. E., and Kraft, R. E., "*Design and Performance of Duct Acoustic Treatment*", Aeroacoustics of Flight Vehicles: Theory and Practice, Volume 2: Noise Control, edited by H. H. Hubbard, NASA Langley Research Center, Hampton, VA, 1991, pp. 165–206.